LA-UR-19-29744
Approved for public release; distribution is unlimited.

Title: FY2019 ASC Physics Validation report: A validation assessment of the xRAGE laser package in 1d using Michel2013

Author(s): Wilson, Brandon Merrill
Koskelo, Aaron C.

Intended for: Report

Issued: 2019-09-26

Disclaimer:
Los Alamos National Laboratory, an affirmative action/equal opportunity employer, is operated by Triad National Security, LLC for the National Nuclear Security Administration of U.S. Department of Energy under contract 89233218CNA000001. By approving this article, the publisher recognizes that the U.S. Government retains nonexclusive, royalty-free license to publish or reproduce the published form of this contribution, or to allow others to do so, for U.S. Government purposes. Los Alamos National Laboratory requests that the publisher identify this article as work performed under the auspices of the U.S. Department of Energy. Los Alamos National Laboratory strongly supports academic freedom and a researcher's right to publish; as an institution, however, the Laboratory does not endorse the viewpoint of a publication or guarantee its technical correctness.

FY2019 ASC Physics Validation report: A validation assessment of the xRAGE laser package in 1d using Michel2013

Brandon M. Wilson and Aaron C. Koskelo
XCP-8: Verification and Analysis

September 25, 2019

Executive Summary

In this report we use standard V&V methodologies to assess the current implementation of the laser-package in xRAGE. Validation assessment of the laser package is currently limited to single-shell, laser-driven, direct-drive experiments from the Omega laser facility (see Michel *et al.* [30]).

Rigorous evaluation was conducted to quantify model accuracy, confidence, and acceptability. Based on the assessment evaluation, several recommendations are suggested regarding model-usage and resource allocation:

Model Usage

- The current xRAGE/Mazinisin implementation has a model form error (likely CBET).
    1. unmodeled nonlinear LPI, such as cross-beam energy transfer (CBET),
    2. insufficient laser deposition during the first laser picket,
    3. neglect of NLTE opacity.
- The ablation front velocity validation is ambiguous due to large experimental uncertainties.
- Common CBET mitigation techniques improve model accuracy.
    - However, these are based on weak physics bases and are calibrated at the expense of predictability.
    - The laser-scaling calibration is more physically-based and improves QoI across the board
- The model is insensitive to many modeling choices.
    - The model agrees with non-local thermal conduction with a flux limiter 0.03.
    - The model is insensitive to partial ionization, Sesame EOS, and NLTE.

Resource Allocation

- Include CBET capabilities in the xRAGE laser package (Mazinisin).
- Supplement HEDP-VS with experiments that address
    - CBET sensitivity experiments
    - LPI experiments during the first picket

This work has resulted in the publication of several reports, articles, and presentations at both internal and external venues:

Invited Talks and Conference Presentations

1. Wilson *et al. Development of the xRage High Energy Density Physics Validation Suite (HEDP-VS)*. Omega Laser User Group Meeting, April 2018 (LA-UR-18-23435).
2. Wilson *et al. Development of the xRage High Energy Density Physics Validation Suite (HEDP-VS)*. ASME Verification and Validation Symposium, May 2018 (LA-UR-18-24066).
3. Wilson *et al. Assessing xRAGE predictive capabilities using the high-energy-density physics validation suite (HEDP-VS)*. Anomalous Absorption Conference, July 2018 (LA-UR-18-25821).
4. Koskelo *Initial Thoughts on Advanced Capabilities for V&V UQ Procedures: LANL*. ASC V&V UQ Workshop, LLNL, August 2018 (LA-UR-18-00789).
5. Wilson *et al. Assessing xRAGE Predictive Capability using the High-Energy-Density Physics Validation Suite*. NECDC 2018, October 2018 (LA-UR-18-29173).
6. Wilson *et al. Assessing xRAGE predictive capability using the high-energy-density physics validation suite*. Invited Talk, Sandia National Labs, October, 2018 (LA-UR-18-30018).

7. Koskelo *et al. Thoughts on Important Questions in V&V: LANL.* LANL-SNL V&V Informational Exchange Meeting, Sandia National Labs, October, 2018 (LA-UR-18-31256).
8. Koskelo *et al. Considerations for verification, validation, and uncertainty quantification (VV&UQ) in high-energy-density physics simulations.* APS DPP, November, 2018 (LA-UR-18-30560).
9. Kline *et al. Scaling of High Energy Density Physics experiments.* APS DPP, November, 2018 (LA-UR-18-30664).
10. Wilson *et al. Towards designing high-energy density physics experiments for model validation.* APS DPP, November, 2018 (LA-UR-18-30578).
11. Haines *et al. Uses of LLE Ray Trace in xRAGE.* LLE Visit, April 2019 (LA-UR-19-22999).
12. Wilson *et al. Development of a statistically-based validation assessment framework to quantify model confidence, model acceptability, and validation recommendations.* ASME V&V Symposium, May 2019 (LA-UR-19-24352).
13. Wilson *et al. Submission to the V&V Symposium Challenge Problem: Workshop on the Assessment of Multivariate Metric for Validation at Multiple Set Points.* ASME V&V Symposium, May 2019 (LA-UR-19-23857).
14. Wilson *et al. Validation Assessment of the xRAGE laser package: Development of a validation workflow designed to meet stakeholder's requirements.* XCP Seminar, August 2019 (LA-UR-19-27420).

Journal Articles, Proceedings, and Reports

1. Wilson *et al. Validation of the xRage laser package* FY2017 Physics Validation L2 Milestone, September 2017 (LA-UR-17-28209).
2. Wilson *et al. Assessment of model confidence of a laser source model in xRAGE using Omega direct-drive implosion experiments.* J. VVUQ, December 2018. (LA-UR-18-31895).
3. Wilson *et al. Assessing xRAGE capabilities using the high-energy-density physics validation suite.* NECDC Proceedings, January 2019 (LA-UR-19-20329).
4. Wilson *et al. A Practical Validation Assessment Workflow.* J. VVUQ, submitted (LA-UR-19-29223).
5. Wilson *et al. The use of hypothesis testing for model acceptability and validation evaluation for a laser source model in xRAGE using Omega direct-drive implosion experiments.* J. VVUQ, in preparation (LA-UR-19-XXXXX).
6. Wilson *et al. Validation Evaluation ....* J. VVUQ, in preparation (LA-UR-19-XXXXX).
7. Wilson *et al. Comparison of validation metrics ....* J. VVUQ, in preparation (LA-UR-19-XXXXX).

1 Introduction

xRAGE [13], a multiphysics code at Los Alamos National Laboratory (LANL), is increasingly being used to study high-energy-density physics (HEDP). HEDP is a realm of physics with applications in astrophysics (*e.g.* supernova [11]), fusion energy physics (*e.g.* inertial confinement fusion (ICF) [4]), and engineering (*e.g.* exploding wires and solid target laser interactions). The study of HEDP relies heavily on modeling and simulation due to its complexity and strong coupling of multiphysics, including radiation transport, hydrodynamics, opacities, and plasma physics (see Atzeni and Meyer-Ter-Vehn [3])

Recent advances [16] have improved xRAGE capabilities to include HEDP and ICF applications. One significant update is the addition of a ray-tracing laser package Mazinisin [28], developed at the Laboratory for Laser Energetics (LLE). The Mazinisin ray-trace package is already coupled to the LLE multiphysics code DRACO [21]. Similar implementations of laser ray-tracing packages already exist in other multiphysics codes, such as LILAC (LLE, [15]) and Hydra (Lawrence Livermore National Laboratory (LLNL), [22]).

With the laser package, improved prescription of energy deposition boundary conditions from laser facilities (*e.g.* National Ignition Facility (NIF) and Omega) is expected. This will impact LANL's predictive capability in HEDP research, such as direct-drive and indirect-drive ICF, opacity characterization, and foil ablation.

A primary concern at LANL is quantifying our statistical confidence in code and model predictability through verification, validation, and uncertainty quantification (VV&UQ) and has led to the development of the HEDP Validation Suite (HEDP-VS). Initial verification of the laser package implementation in xRAGE has been performed by Haines *et al.* [17], Wilson *et al.* [42], and Bradley *et al.* [6, 5].

This work presents the validation assessment of xRAGE coupled with Mazinisin to predict single-shell, laser-driven spherical implosions relevant to direct-drive ICF. In Section 2, we give a brief background into the validation methodologies and definitions used in this analysis. We provide a short description of the Michel2013 experiment and xRAGE simulation details and configuration in Section 3.1 and 3.3, respectively. This is followed by the validation assessment, in which, model accuracy, confidence, and acceptability are quantified (Sections 3.4 and 3.5, respectively). A rigorous validation evaluation is given in Section 3.6 and recommendations, based on the validation assessment, are proposed in Section 3.7. In the final sections (Section 4.2-4.3), current and developing validation addressing the validation recommendations is presented.

2 Validation Methodology and Definitions

In this paper, we use the methodology presented by Wilson and Koskelo [38, 39, 41, 40, 37] to quantify model accuracy, confidence, and acceptability along with validation evaluation and recommendations. For clarity, the definitions of these are given:

Model Accuracy *Determination of a model's accuracy for a set of model prediction QoI as compared to experiment.*

Model Confidence *Quantification of the degree of confidence in a model's accuracy.*

Model Acceptability *Statistical acceptance or rejection of a model given validation evidence (i.e. model accuracy and confidence) and model requirements based on the intended uses of the model.*

Validation Evaluation *Quantitative evaluation of the model, experiment, and validation process based on the intended use and predictive applications of the model*

Validation Recommendations *Recommendations intended to guide future validation strategies, resource allocation, model-use, and prioritization of validation investments*

In this paper, we use the standard methodology (see the ASME V&V 20 Standard [2]) to quantify model accuracy and confidence. In particular, we use the ASME V&V 20 Standard [2] to 1) quantify our validation uncertainty, including numerical, model input, and experimental uncertainties (Section 3.6.4), 2) determine our model confidence (Section 3.4), and 3) qualitatively interpret our validation results.

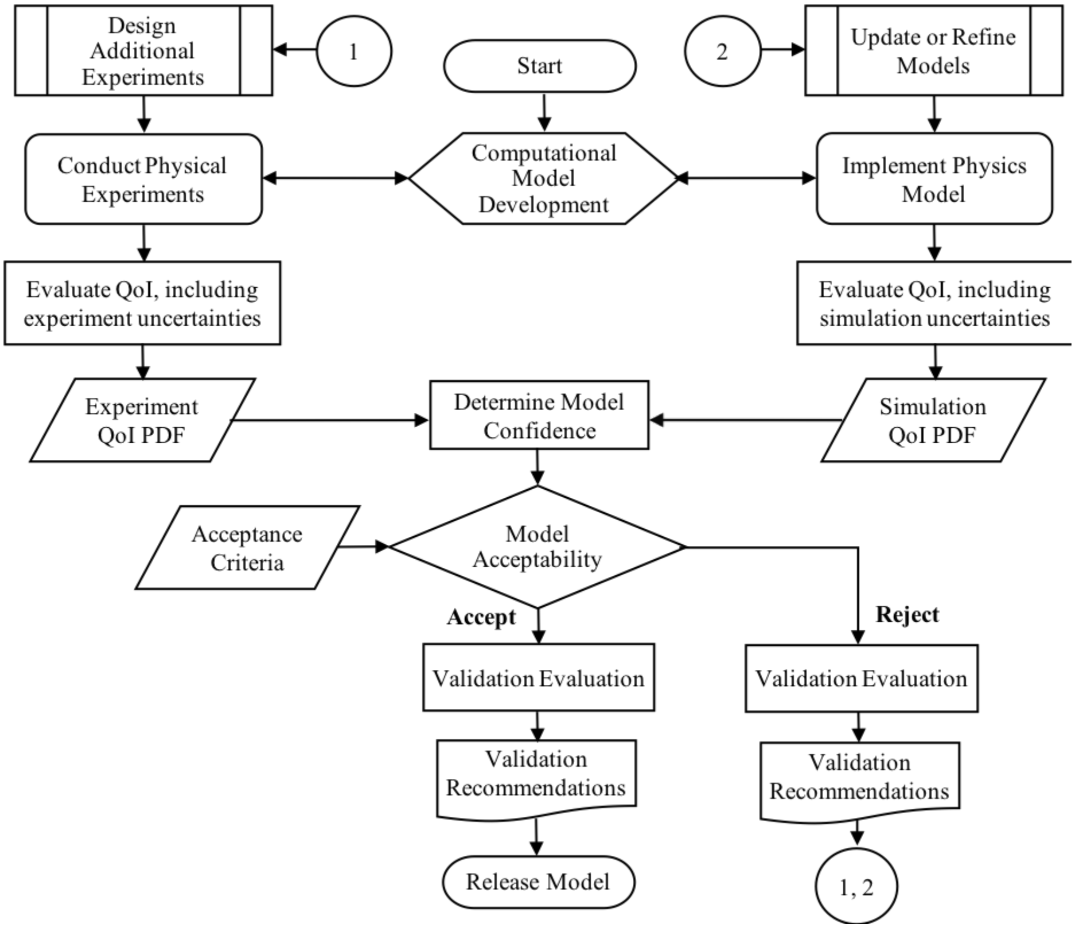
Design Additional Experiments
1
Start
2
Update or Refine Models
Conduct Physical Experiments
Computational Model Development
Implement Physics Model
Evaluate QoI, including experiment uncertainties
Evaluate QoI, including simulation uncertainties
Experiment QoI PDF
Determine Model Confidence
Simulation QoI PDF
Acceptance Criteria
Model Acceptability
Accept
Reject
Validation Evaluation
Validation Evaluation
Validation Recommendations
Validation Recommendations
Release Model
1, 2

Figure 1: Workflow for a comprehensive validation assessment, including model accuracy, confidence, acceptability, and validation recommendations.

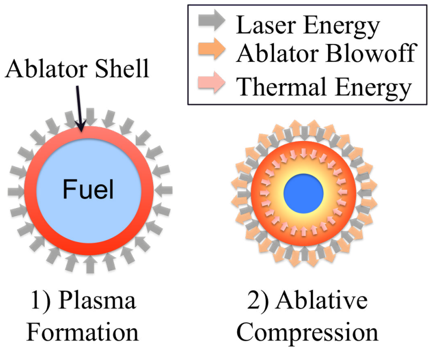

Figure 2: Early implosion dynamics of a typical ICF validation experiment. First, significant energy from high energy lasers is absorbed into the capsule ablator shell via inverse bremsstrahlung. Next, the outer shell ablation accelerates the shell inward and compresses the fuel and inner layers to very high temperatures and pressures.

3 Validation Assessment of Michel2013

ICF plays a significant role in understanding, achieving, and developing a sustainable fusion energy source. Examples of facilities with a focus on ICF research include Omega at LLE, NIF at LLNL, and Z-machine at Sandia National Laboratory. Although many approaches are available, in this paper we focus on laser-driven, direct-drive ICF experiments at Omega. A brief background into inertial confinement fusion follows, but the reader is referred to more detailed works in the literature *e.g.* Atzeni and Meyer-Ter-Vehn [3], Craxton *et al.* [8], and Lindl *et al.* [24].

In laser-driven, direct drive ICF, high-energy lasers implode a small capsule with radius $r_o \leq 500\mu$m. This compresses the a deuterium-tritium fuel mixture contained within the capsule to extreme pressures ($>$ 1Mbar), densities (≥ 200g/cm^3) and temperatures (1×10^8K). When the fuel is sufficiently compressed, it ignites initiating thermonuclear burn and nuclear fusion yield.

Laser-driven, direct drive ICF is a complex, dynamic process wherein different physical processes interact and couple. To perform a hierarchical validation assessment to assess the validity of a computer model simulation of the overall process from start to finish, one starts with the initial conditions generated by the absorption of laser energy on the capsule (see Fig. 2). The simulation validation conducted here is concerned only with the early implosion hydrodynamics, before particle transport and nuclear burn physics become important.

During early implosion, the laser beams deposit significant energy ($>$ 10TW) into the capsule outer material layer (ablator shell) and ionize the ablator shell. In the under-dense plasma, the laser energy is absorbed and scattered through diverse laser-plasma interactions (LPI), but is, primarily, absorbed through inverse bremsstrahlung. The absorbed portion of the incident laser energy is conducted via electrons and radiation from the critical surface to the ablation front and provides the energy required to accelerate the plasma capsule inward, much like the effect of a rocket. An example of the density and temperature profiles at the ablation front is shown in Fig. 5.

In identifying viable validation experiments, we chose well-characterized, documented experiments in which the experimental measurements and laser physics are not significantly coupled to other physical mechanisms. This was difficult due to the inherent coupling of many multiphysics processes that exist during high-energy laser deposition, such as plasma physics, x-ray emission, material opacities, linear and nonlinear light scattering, electron-ion coupling, and hydrodynamics [8].

For this paper, we chose the experiments found in Michel *et al.* [29, 30] and include them in the HEDP-VS. These experiments consist of direct drive implosions of single-shell capsules (see Fig. 4 and 5 in Michel *et al.* [29]. We include the Michel *et al.* [29, 30] experiments as they demonstrate many desirable aspects for validation experiments, including

1. decoupling of laser physics (laser source) from system response,

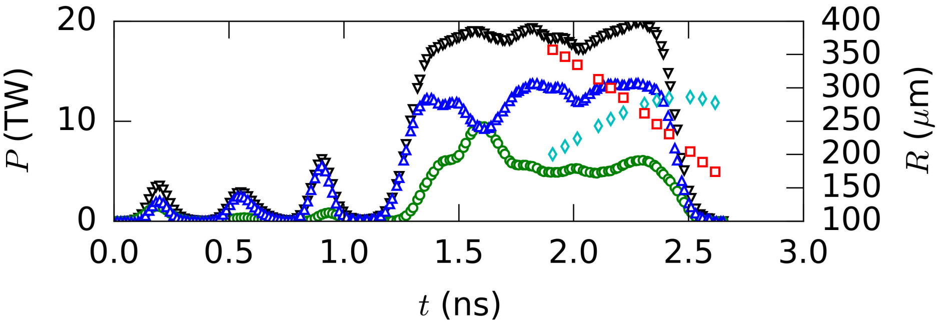

Figure 3: Example of the experimental data for the Be (high) case. QoI shown are the laser energy (▽), scattered energy (○), absorbed energy (△), ablation front position (□), and ablation front velocity (◊). Uncertainties are on the order of symbol size.

2. simple experimental configuration,
3. comprehensive range of laser energies and ablator materials with experimental replicates, and
4. well-characterized measurements and uncertainties for model inputs and quantities of interest (QoI).

3.1 Experimental Configuration

The experiments in Michel *et al.* [29, 30] were configured similar to the diagram in Fig. 2 with air replacing the deuterium-tritium fuel. The purpose was to investigate how the ablator material interacts with the laser and transfers energy to create the early implosion hydrodynamics of the inner shell. Each experiment includes well-characterized, time resolved measurements of the incident and scattered laser energy and ablator shell dynamics. The experiments are briefly described; however, for complete details about the experimental setup and diagnostics, the reader is referred to Michel *et al.* [29, 30].

Fig. 3 shows QoI for a representative experiment during implosion. A 60 beam, nearly uniform laser pulse preceded by three preliminary pulses (black symbols in Fig. 3) wth peak power just under 20TW drives a spherical capsule inward on a preferred adiabat. Laser scattering (green symbols in Fig. 3) was measured using a calorimeter. A significant portion ($\approx 30\%$ of the laser energy is scattered through linear and nonlinear processes. The ablation front is rapidly driven to the capsule center; the position and velocity of the ablation front were measured from self-emission x-rays captured on a framing camera and are shown in Fig. 3 as red and cyan symbols, respectively. Toward the end of the laser drive, the ablation front is observed to decelerate as the inward propagating shell encounters the reflected shock.

Three ablator shell materials (Be, CH, and C), and two laser energy profiles (which are denoted high and low energy) are investigated, providing six experimental cases [30]. Nominal values and uncertainties for the laser and capsules are given in Appendix B. These are also inputs to the simulation.

3.2 Diagnostics

Several diagnostics capture the laser drive physics QoI - see Table 1. The incident laser power P_i is measured upstream of the target interaction during drive. The total scattered laser energy is measured using time-integrated calorimeters. Temporally-resolved, relative scattered spectra are also captured using a high-dynamic range (HDR) streak camera multiplexed into a spectrometer.

Calorimeter measurements are used to scale relative energy measurements from the streak camera to the total scattered energy giving temporally-resolved scattered power P_s (see Fig. 3). The triple picket pulse at $t \approx 0.3$, 0.6, and 0.9ns followed by a long step pulse is observed. A significant portion ($\approx 30\%$) of the incident laser energy is scattered through linear and nonlinear processes. The absorbed laser power P_a by the capsule is calculated as the difference of the incident and scattered laser power.

Additionally, a 1 keV x-ray framing camera (XRFC) captures the soft x-ray self emission from the ablator shell [30]. At these photon energies, a maximum intensity is created in the coronal plasma by the limb effect. However, optically thick, cold, dense material interior to the ablation front causes a sharp gradient of the signal intensity. On the basis of simulations, the mid-point of this internal gradient was found to indicate the position R and velocity v of the ablation front [30].

In addition to these QoI, the energy spectrum of scattered wavelengths was also measured using the HDR streak camera. The scattered wavelengths cannot currently be captured with the current simulations, so no comparison will be made. However, this is a metric that would better inform validation assessment in the future.

The uncertainties suggested in Table 1 make up the experimental uncertainties for the validation assessment shown in Fig. 3.

3.3 xRAGE Simulation Configuration

For validation, a one dimensional (1d) spherical geometry is set up to match nominal experimental conditions as best as can be interpreted from the experimental description. Three ablator shell materials (*i.e.* CH, Be, and C) are simulated at two laser energy magnitudes, denoted later as low (l) or high (h). The as-measured incident laser drive energy profile, initial capsule outer radii, and capsule mass are used as simulation inputs (see Appendix B).

Solutions are calculated using the LANL Eulerian multiphysics code xRAGE coupled with the laser package Mazinisin. The governing physics and coupled physics packages are described in subsequent sections.

3.3.1 Calculation Control

Simulations are run nearly to the minimum implosion diameter. This corresponded to 3.5ns (low) and 3.0ns (high). The nominal initial timestep is set to 8×10^{-8}ns but additional studies indicate negligible sensitivity to this value. Nominal run times are approximately 4.5hrs on 16 processor cores. While running, output files were written every $n_{dump} = 2000$ cycles.

xRAGE processing of the 1d simulations took place on 16 nodes of LANL's Snow high performance computing (HPC) resource. Snow uses Intel Xeon Broadwell CPU's with 36 cores and 128 GB of memory per node. Simulation results were similar for other LANL HPC architecture (*i.e.* Moonlight).

Simulation sensitivities to calculation control are negligible. See Appendix C for more details.

3.3.2 Mesh and Geometry Definition

The model geometry consists of a spherical 1d ablator shell (shown in Fig. 4) with nominal outer radius $\tilde{r}_o$ and mass $\tilde{m}_a$ (see Appendix B). The deviations of the radius and mass from nominal are parameterized such that the remaining geometric values (*i.e.* inner radius r_i, thickness t_a) can be calculated:

$$t_a = r_o - \left((r_o)^3 - \frac{m_a}{4/3\pi\rho_a} \right)^{1/3}, \quad r_i = r_o - t_a. \tag{1}$$

where ρ_a is the ablator density and $r_o = \tilde{r}_o + u_{r_o}$ and $m_a = \tilde{m}_a + u_{m_a}$ are sample realizations of a nominal quantity combined with a random deviation. This definition is particularly useful when determining sensitivities and Monte-Carlo sampling.

Air at a partial vacuum (1×10^{-4}g/cm^3) occupies the region both inside and outside the capsule. Prior to implosion, all materials are assumed to be at room temperature (0.0257eV). Errors due to these assumptions are included in the input uncertainty quantification.

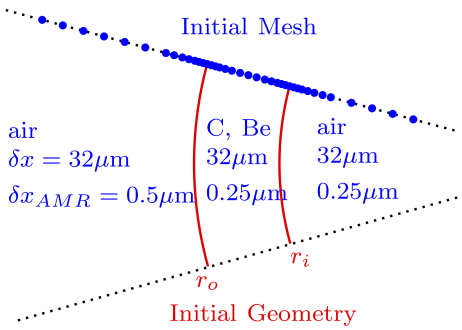

Figure 4: The initial mesh (top) and geometry (bottom) given to xRAGE. To better show the capsule geometry, the geometry scale is exaggerated. Mesh spacing is realistic.

The xRAGE hydrodynamic mesh does not track material interfaces, but, instead, allows multiple materials per mesh cell through volume averaging the material properties. Note that while interfaces are not tracked by the mesh, interfaces are preserved by the hydrodynamics algorithm (see below). The nominal initial 1d Eulerian mesh contains 400 cells with an initial size of $\overline{\delta x} = 32\mu$m.

At the first iteration, adaptive mesh refinement (AMR) refines the initial xRAGE mesh at cells that meet the predefined xRAGE refinement criteria (shown in Fig. 4). Default refinement criteria include high spatial gradients in density and pressure, the magnitude of the jump in partial density across a material interface, and the compression of a cell at the current time step [10]. Nominally, we limit AMR to a minimum refinement of $\delta x_{AMR} = 0.25\mu$m from the capsule outer radius inward and $\delta x_{AMR} = 0.5\mu$m outside the capsule resulting in a late-time mesh significantly refined beyond the nominal mesh in Fig. 4. *When investigating mesh sensitivity, uniform refinement criteria are applied to the initial mesh size and AMR minimum refinement parameters.*

The laser package requires a secondary mesh for ray-tracing. As recommended in xRAGE documentation [10], the laser package mesh uses the hydrodynamics mesh refined by a factor of two.

3.3.3 Plasma Model

We use the xRAGE three temperature (3T) model, which solves the Euler hydrodynamic transport, electron and ion specific internal energy evolution (electron-ion coupling), electron-radiation coupling, and radiation-diffusion equations.

Hydrodynamics calculations solve the Euler hydrodyamic transport equations. The numerical algorithm which solves the Euler equations uses an interface preservation technique with a shock detector that does not affect the volume fraction and a modified Van Leer limiter for reconstruction of primitive quantities. Thermal conductivity and electron coupling are also turned on.

Transport of energy via radiative processes is modeled using multigroup radiation diffusion with a Levermore flux limiter [36]. This is an approximation to the computationally expensive, full, angular-dependent radiation transport equation.

3.3.4 Electron Thermal Conduction

The Lee-More modification of the Spitzer-Harm model is used to model electron thermal conductivity. A thermal flux limiter is used to adjust the Spitzer-Harm [36] electron thermal conduction. Suggested thermal flux limiter magnitudes range from $0.5 \leq f \leq 1.0$ [36] for most radiation diffusion problems and $0.03 \leq f \leq 0.1$ [27] for direct-drive cases. Flux limiter values of $f \approx 0.06$ are suggested for xRAGE [10]. We discuss optimal thermal flux limiter magnitudes and validation metric sensitivities to the thermal flux limiter in more detail in Section C.1.

Local thermal transport models (such as the Spitzer-Harm model) break down when thermal gradient length scale and thermal electron mean-free path are of similar magnitude. These conditions can be significant at high laser intensities ($\approx 10^{15}\mathrm{W/cm^2}$) [18]. Instead, a non-local thermal transport model can account for deeper penetration of thermal electrons by extending the Spitzer-Harm current over several electron mean-free paths [10].

When investigating non-local effects, we use the Schurtz model [35]. All validation results use the local thermal transport model due to the high computational cost of a non-local thermal transport model. However, results are compared against the non-local Schurtz model for select runs. The comparison indicates a local thermal transport model with $f \approx 0.6$ captures all relevant physics.

3.3.5 Materials and Opacities

Material equation of state (EoS) are obtained from the SESAME EoS tables [25] for Be, C, and air.

Opacities based on assumptions of local thermodynamic equilibrium (LTE) are calculated using TOPS [26]. The calculations are based on multigroup thermal diffusion using 60 groups or bins of photon energies logarithmically spanning 1×10^-3 to 1.5×10^2keV. Materials are separated into their primary elements for characterization of LTE opacities. Multiple runs have demonstrated is model is insensitive to the resolution of multipgroup diffusion beyond 60 groups. Although ICF laser and plasma physics often require non-local thermal equilibrium (NLTE) opacity definitions, these are not yet implemented in the current code for our materials of interest. It is also worth noting NLTE is often not investigated for modern direct-drive simulations.

3.3.6 Ion Physics

Isotopics for air and ablator shell materials are defined to calculate effects of partial ionization within the growing ablation front. Partial ionization is modeled using the Zimmerman implementation of the Thomas-Fermi ionization model. The simulations are insensitive to full and partial ionization definitions derived from lookup tables, such as SESAME and TOPS.

3.3.7 Laser Package

One of the purposes of this validation suite is to validate the laser package capabilities within xRAGE. The laser package derives from LLE's Mazinisin laser ray-trace package [28] and predicts laser deposition through inverse-bremsstrahlung.

The laser configuration matches that of the Omega laser facility and the conditions in Michel *et al.* [30]. The beam radius ($1/e^2$) is 353μm with a 4th order super-Gaussian spatial profile, commensurate with known Omega beam profiles. The temporal profile is defined by the experimentally measured time-dependence of the incident laser energy. For the Mazanisin definition, a cold start (direct-drive), sector ray-trace configuration is enabled with 10 ray groups of 200 rays. The laser package response is insensitive to reasonable variations of the laser drive definition.

Cross beam energy transfer (CBET) [20] is a dominant nonlinear laser plasma interaction in direct-drive ICF that is not currently supported in the xRAGE laser package. We anticipate fully supported CBET models will be implemented in the next version of the xRAGE laser package. To date, LLE's DRACO [21] is the only multiphysics code that has demonstrated CBET predictive capabilities in its ray-trace laser package.

3.3.8 Validation QoI

The validation QoI of interest include the scattered laser energy and position and velocity of the ablation front trajectory. Subtle, yet perhaps significant, differences exist in post-processing between experiment and simulation. This introduces a comparison uncertainty not explicitly addressed in ASME V&V 20-2009 [2].

In the experiment, incident energy ϕ_{p_i} and scattered energy ϕ_{p_s} are directly measured. However, the simulation predicts the capsule absorbed energy ϕ_{p_a}. The scattered energy is derived as the incident and absorbed energy difference (*i.e.* $\phi_{p_s} = \phi_{p_i} - \phi_{p_a}$). Although the absorbed energy is usually the design QoI, we will only discuss

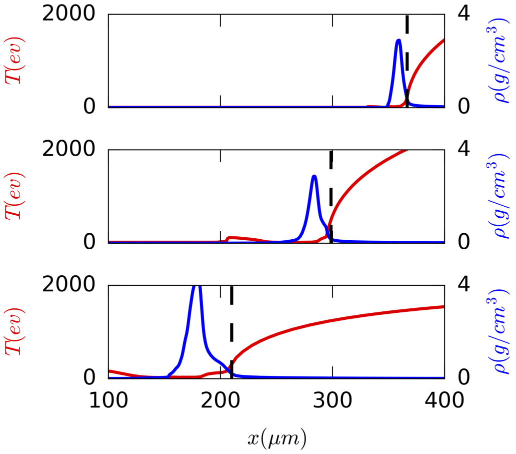

Figure 5: Electron temperature and density profiles at 1800ps (top), 2200ps (middle), and 2600ps (bottom) during the drive for the high energy Be ablator shells. Ablation front is indicated by vertical dashed line. As time progresses, a dense plasma separates the ablation front from the bulk mass.

validation for scattered energy. Validation of ϕ_{p_a} can be determined from the above algebraic relationship of scattered and incident energy.

The ablation front trajectory ϕ_r is identified from the x-ray self-emission images as the half-intensity location of the steep inner edge caused by the limb effect [30]. In the simulation, the ablation front is easily identified at each timestep by locating the position of the temperature inflection within the ablation region. The identified ablation front is shown alongside the temperature and density profiles for the xRAGE simulation at 1.6, 2, and 2.4ns in Fig 5. To reduce noise introduced by numerical differentiation, a 4th order, least-squares polynomial fit of the ablation front position is used to determine the ablation front velocity ϕ_v.

Ablation front QoI are strongly coupled to other modeled physical mechanisms (*e.g.* material opacities, EoS, radiation diffusion, etc.). Prediction of ablation front QoI is challenging due to coupled multiphysics and increases in difficulty due to error propagation with higher-order derivatives.

Comparison of the QoI for the high energy cases are shown in Fig. 3. Results in Fig. 3 use nominal values for geometry, material, and simulation parameters. The scattered laser energy is underpredicted (consequently, the absorbed energy is overpredicted). Further assessment follows in Section 3.6.

3.4 Model Accuracy and Confidence

Model accuracy and confidence form the validation basis for a validation assessment. In this paper, we follow the ASME V&V standards [1, 2] to quantify model accuracy and confidence. Model accuracy and confidence are determined by the predictive accuracy $\delta_{model,\phi}$ for a set of QoI $\phi = [\phi_1, \phi_2, ...\phi_i, ...\phi_n]$, where subscripts denote individual QoI. For this paper, our QoI consist of $\phi = [\phi_{p_s}, \phi_r, \phi_v]$ *i.e.* scattered laser energies and ablation front trajectory and velocity, respectively.

From V&V 20-2009 (see Fig. 6 for reference), the comparison error e_ϕ is the difference between simulation QoI ϕ_S and experimental QoI ϕ_D (*i.e.* $e_\phi = \phi_S - \phi_D$). For any validation, e_ϕ is probabilistic and belongs to a pdf of possible comparison error responses, i.e. *pdf* (e_ϕ) distributed about the comparison error $\langle e_\phi \rangle$. The pdf of e_ϕ is the convolution of the experimental and simulation QoI probability distributions functions (i.e. *pdf* (ϕ_D) and *pdf* (ϕ_S). The shape and position of each pdf is sensitive to the QoI variability, random errors, and systematic errors, such as

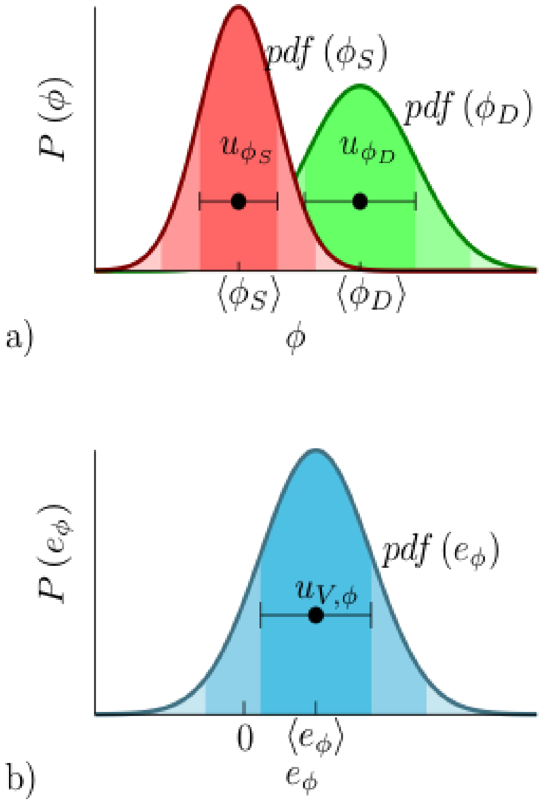

Figure 6: Metrics from the V&V 20-2009. Comparison of simulation and experimental QoI are shown in a), while the comparison error metric is shown in b). Comparison of scattered laser light (green), shell trajectories (red), and shell velocities (cyan) for experimental data (symbols) [29] and xRAGE (lines). Validation uncertainty (*i.e.* 1σ, 2σ, and 3σ confidence) given as shaded regions. Incident laser power (black) is shown as a reference.

numerical discretization error, model input variability, and experimental errors.

The comparison error $\langle e_\phi \rangle$ can be thought of as the accuracy of the model to predict reality and the distribution $pdf\ (e_\phi)$ is our uncertainty on e_ϕ. Herein, we refer to $\langle e_\phi \rangle$ as model accuracy and the distribution of e_ϕ as model confidence, i.e. $pdf\ (e_\phi)$. A point other than the expectation value of $\langle e_\phi \rangle$ could be used for "model accuracy" if appropriate for the application of interest.

In general, the model confidence distribution $pdf\ (e_\phi)$ is unknown. Instead, the error magnitude can be estimated using interval-based uncertainty quantification (see ASME V&V 20-2009 [2]):

$$\delta_{model,\phi} \geq pdf\ (e_\phi) \approx e_\phi \pm u_{V,\phi}, \tag{2}$$

where the validation uncertainty $u_{V,\phi}$ quantifies the uncertainties accumulated during the entire validation process. ASME V&V 20-2009 [2] outlines the appropriate combination of uncertainty components $u_{x,\phi}$, in which

$$u_{V,\phi} \approx \sqrt{\sum_x u_{x,\phi}^2}. \tag{3}$$

This formulation follows from the convolution of multiple uncorrelated, independent gaussian distributions, e.g. *pdf* (ϕ_D) and *pdf* (ϕ_S) (see Lemons [23]).

It is also worth noting these validation results are only applicable to the parameter space and QoI covered by the validation suite. Extreme caution is required when extrapolating validation results outside the region of validation relevancy.

3.4.1 Validation Uncertainty

The ASME V&V 20-2009 standard decomposes validation uncertainty $u_{V,\phi}$ into three components:

1. **Experimental Uncertainty** $u_{D,\phi}$
   Uncertainty from experimental facility, operations, or diagnostics.
2. **Numerical Uncertainty** $u_{N,\phi}$
   Uncertainty from converting a mathematical model to a numerical model.
3. **Input Uncertainty** $u_{I,\phi}$
   Uncertainty on simulation result due to model inputs, such as boundary conditions, material properties, or initial conditions.

The uncertainty magnitude for each component is rigorously quantified and discussed in Section 3.6. For all assesments, we propagate uncertainty confidence intervals (CI) by assuming a Gaussian distribution and coverage factor k. That is, $u_{V_{CI},\phi} = k u_{V_{68\%},\phi}$ where $u_{V_{1\sigma},\phi}$ denotes the standard uncertainty, and the coverage factor $k = 1$, 2, and 3, for the uncertainty confidence interval 68% (standard), 95%, and 99.7% confidence, respectively.

3.4.2 Nominal Model

The nominal model uses the as-measured incident laser energy and a local thermal transport nominal flux limiter of $f = 0.06$ as suggested by Igumenshchev [20] and xRAGE laser package developers [16]. The flux limiter suggested by the xRAGE user manual for ICF applications as determined by calibration [10] corresponds to $f = 0.0231$.

Validation results are shown in Fig. 7. Uncertainties for each QoI are given as shaded regions designating 1σ, 2σ, and 3σ confidence levels. The experimental data shows a significant portion of the incident laser energy is scattered due to linear and nonlinear processes. The absorbed energy ablates the outer capsule resulting in a blowoff layer, plasma corona, and inward acceleration of the ablation front.

For all cases, the scattered laser energy ϕ_{p_s} is significantly underpredicted, which manifests as increased absorption at the capsule outer surface. This propagates into the trajectory QoI by increasing implosion efficiency and over-accelerating ablation front trajectories.

3.5 Model Acceptability

For this demonstration, we define the model-use tolerances for three quantities of interest (QoI), the scattered light energy ϕ_{p_s}, ablation front trajectory ϕ_r, and ablation front velocity ϕ_v. Model-use tolerances were determined through conversation with developers and designers:

1. $\Delta\phi_{p_s} = \pm 0.025 \max(\phi_{p_i}) \approx 0.5$TW and 0.25TW for the high and low energy cases,
2. $\Delta\phi_r = \pm 0.05 \phi_{D,r} \approx 5\%$ of the experimental ablation front trajectory,

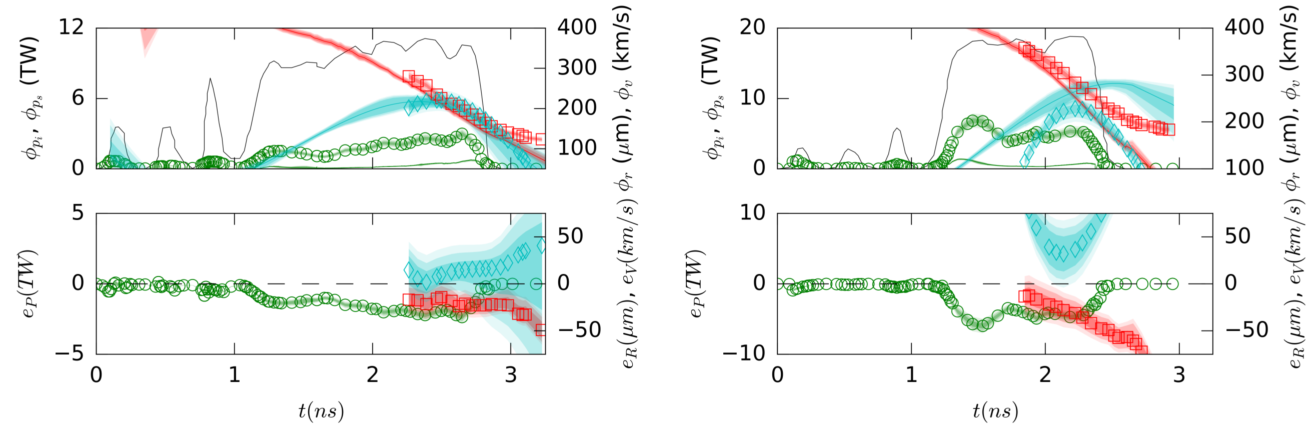

(a) C (l) (b) C (h)

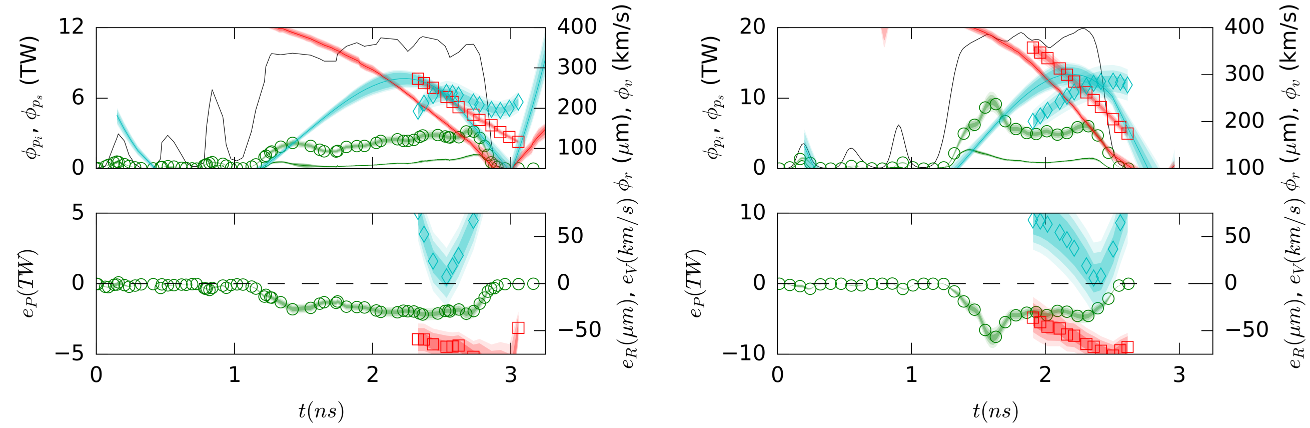

(c) Be (l) (d) Be (h)

Figure 7: Validation assessment of QoI (top) and model error normalized by model requirements (bottom) for the nominal case. Comparison of scattered laser light (green), shell trajectories (red), and shell velocities (cyan) for experimental data (symbols) [29] and xRAGE (lines). Validation uncertainty (*i.e.* 1σ, 2σ, and 3σ confidence) given as shaded regions. Incident laser power (black) is shown as a reference.

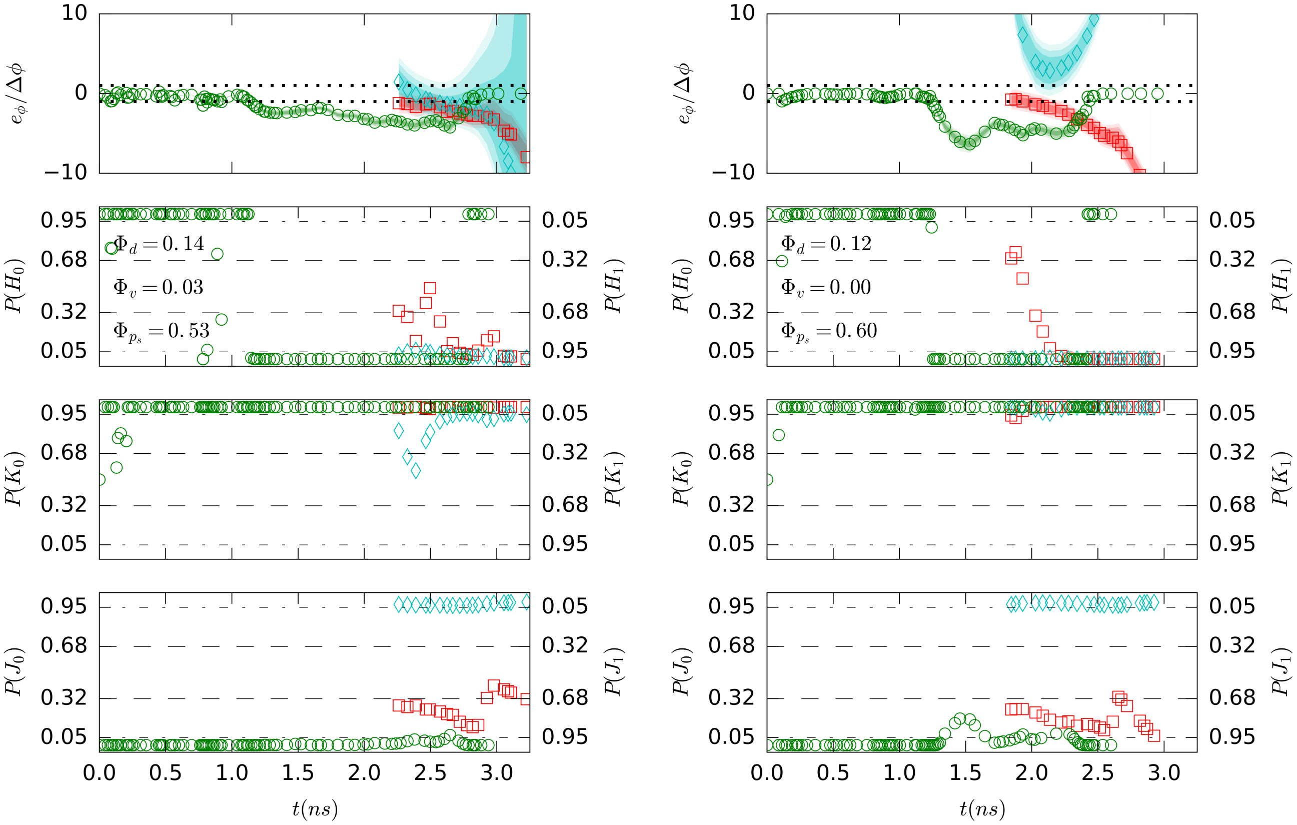

(a) C (l)

(b) C (h)

Figure 8: From top to bottom, model accuracy, model acceptability $P(H_0)$, validation systematic error $P(K_0)$, and validation ambiguity $P(J_0)$ for the validation example in Wilson and Koskelo [38]. QoI correspond to scattered light (green), shell trajectories (red), and shell velocities (cyan). Model confidence (i.e. 1σ, 2σ, and 3σ confidence) given as shaded regions. The region bounding the model-use requirement is shown by dashed lines.

3. $\Delta\phi_v = \pm 0.05\phi_{D,v} \approx 5\%$ of the experimental ablation front velocity.

Model acceptability results for the nominal model validation assessment are given in Fig. 8. The comparison error e_ϕ normalized by the model-use tolerances $\Delta\phi$ provide a reference and basis to formulate a qualitative assessment. The normalized model confidence $(e_phi/\Delta\phi)$ suggests the nominal model suffers from a significant systematic error during the primary drive for all QoI (see Wilson and Koskelo [38]).

This assessment is confirmed by the model acceptability test $P(H_0)$ (shown in Fig. 8-10). During the triple picket pulse, the nominal model is acceptable within our model-use tolerances; However, we can reject the nominal model for all QoI with high confidence ($P(H_1) \geq 0.95$) during the primary drive. Some spurious ablation front trajectory and velocity values indicate an ambiguous rejection, in which, the probability of an acceptable or rejected model is not statistically significant ($0.05 \leq P(H_1), P(H_0) \leq 0.95$).

Causes for rejecting the model may be many, such as model-form errors, large experimental or simulation uncertainties, unresolved numerics, and experimental bias. An extensive evaluation of the cause of the unacceptable model are assessed in validation evaluation (Section 3.6).

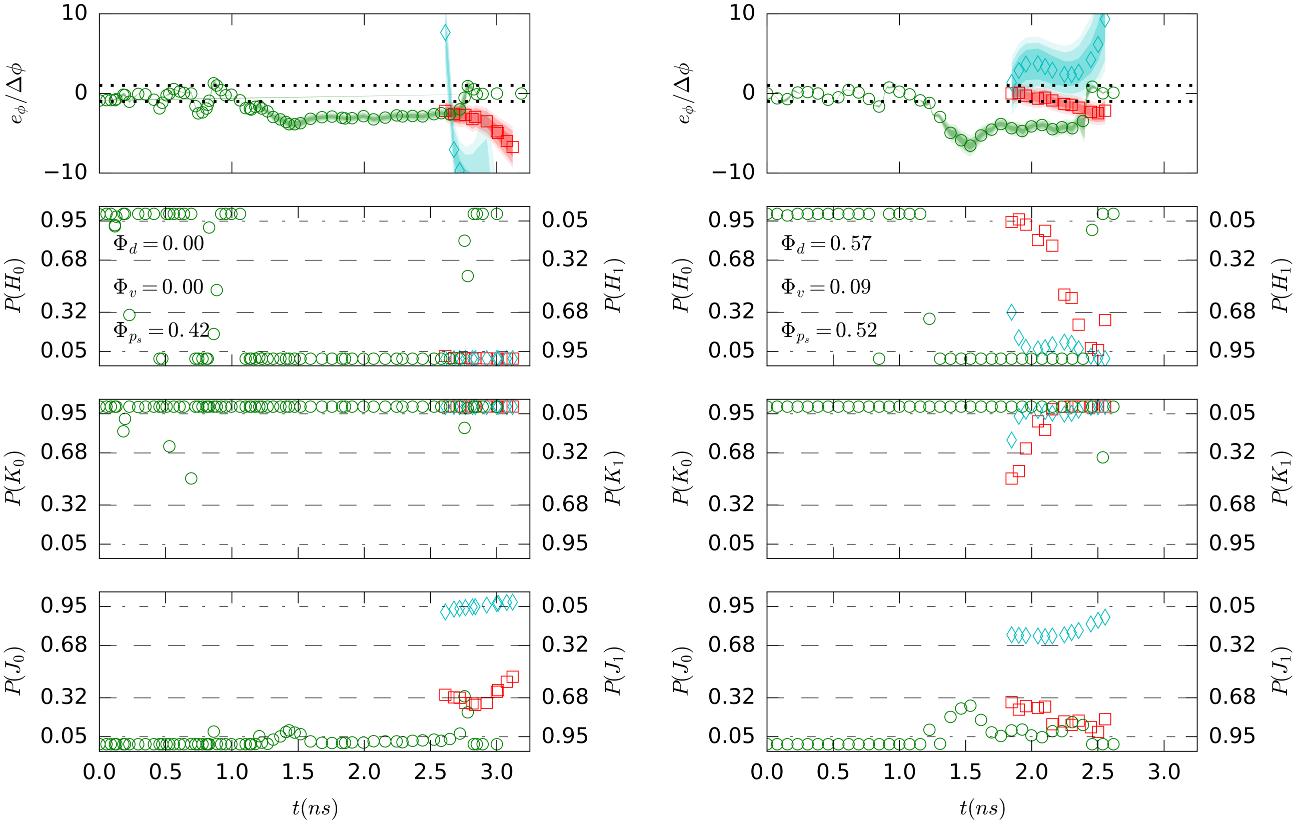

(a) CH (l)

(b) CH (h)

Figure 9: From top to bottom, model accuracy, model acceptability $P\left(H_0\right)$, validation systematic error $P\left(K_0\right)$, and validation ambiguity $P\left(J_0\right)$ for the validation example in Wilson and Koskelo [38]. QoI correspond to scattered light (green), shell trajectories (red), and shell velocities (cyan). Model confidence (i.e. 1σ, 2σ, and 3σ confidence) given as shaded regions. The region bounding the model-use requirement is shown by dashed lines.

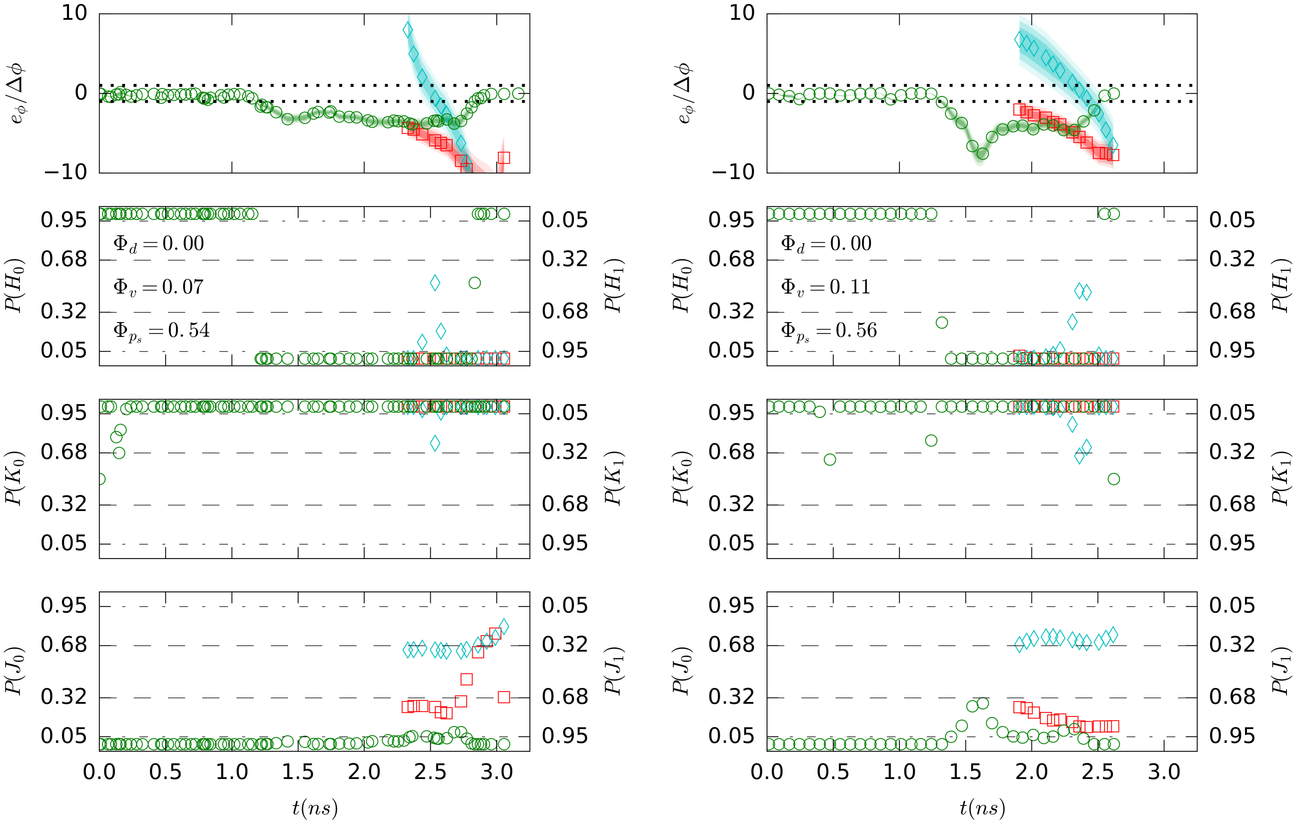

(a) Be (l)

(b) Be (h)

Figure 10: From top to bottom, model accuracy, model acceptability $P(H_0)$, validation systematic error $P(K_0)$, and validation ambiguity $P(J_0)$ for the validation example in Wilson and Koskelo [38]. QoI correspond to scattered light (green), shell trajectories (red), and shell velocities (cyan). Model confidence (i.e. 1σ, 2σ, and 3σ confidence) given as shaded regions. The region bounding the model-use requirement is shown by dashed lines.

3.6 Validation Evaluation

Validation evaluation is meant to provide a quantitative evaluation of the model, experiment and validation process based on the intended use and predictive applications of the model. Two questions we would like to evaluate include

1. What are the sources of an unacceptable model?
2. What physics or model-uses should we be concerned with when using the model as it is used today?
3. How can we improve the model, validation, or experiment in the future?

A wide variety of methodologies should be used. In this section, we address validation evaluation and the above questions using

- hypothesis testing for systematic errors and ambiguity in Section 3.6.1,
- subject-matter expert evaluation for error sources 3.6.2,
- evaluation of model calibration methods in Sections 3.6.3,
- uncertainty contributions and reduction in Section 3.6.4, and
- sensitivity studies of QoI to modeling choices in Section C,

3.6.1 Hypothesis Testing for a Systematic Error and Ambiguity

We use hypothesis testing to indicate the presence of systematic errors or ambiguity in the validation comparison. The hypothesis tests used are outlined in Wilson and Koskelo [39].

The validation hypothesis tests are shown in the bottom plots of Fig. 8-10. *Results suggest the presence of both systematic errors ($P\left(J_0\right)$) and ambiguity ($P\left(K_0\right)$).* We have high confidence ($P\left(K_0\right) \geq 0.95$) all QoI are affected by a systematic error. The ablation front velocity for the low energy, C ablator case is the outlier, in which our confidence in the existance of a systematic error is slightly lower ($P\left(K_0\right) \geq 0.80$).

It is important to remind the reader that a systematic error does not indicate an unacceptable model. For example, the nominal model is acceptable (within our moddl-use tolerances) but, likely, has a systematic error during the triple picket pulse. This could be due to a smaller total uncertainty than the mismatch between experimental and simulation QoI ($\langle e_\phi \rangle$ or model accuracy).

The validation ambiguity ($P\left(J_0\right)$) indicates the ablation front velocity uncertainties are large enough to cause an ambiguous validation. This affect is most severe for the C ablator cases. Ablation front trajectory validation is slightly ambiguous $P\left(J_0\right) \approx 0.25$ and laser scattering is not affected by ambiguity $P\left(J_0\right) \geq 0.1$.

At this point, it is worth evaluating the sources of systematic errors and uncertainty contributions to reduce them in future validation iterations.

3.6.2 Subject Matter Expert Consideration of Systematic Error Modeling Sources

We investigate the sensitivity of QoI to xRAGE submodels (*e.g.* equation of state, partial ionization, etc.) to identify potential sources of model forms. These are discussed in Appendix C. In summary, the simulations are only significantly sensitive to model inputs and models impacting laser energy deposition.

We also identified other sources of systematic errors in the model capabilities through discussion with experimentalist, code developer, and HEDP subject matter experts. The most likely sources of systematic errors are discussed in the following sections.

Insufficient First Picket Energy Deposition

The initial state of the capsule is cold and non-ionized. The interaction of the laser with non-ionized material sets up conditions in which short-lived, non-inverse bremsstrahlung LPI exist. Normally, during a high-energy laser

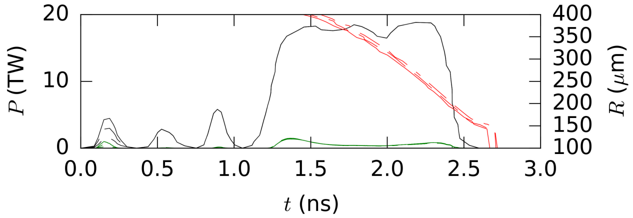

Figure 11: Sensitivity to the laser energy deposited during the first laser picket (*i.e.* $1.5P_{i,t\leq 0.3}$ (—), P_i (——), and $0.5P_{i,t\leq 0.3}$ (—–), respectively. Comparison of laser power (black), scattered laser energy (green) and shell trajectory (red). The results are presented for the C ablator shell at high laser power. Incident laser power (black) is shown as a reference.

step profile, the energy contributions from the short-lived, early-time LPI are much smaller than the total incident energy. However, with a triple picket pulse shape, the short-lived LPI energy contributions or losses are much larger relative to the incident energy.

The laser package only models energy deposited via inverse bremsstrahlung. Energy deposited or scattered by unmodeled LPI processes strongly affect the shock strength and shocked state following the first picket. Consequently, prediction errors during the first picket propagate into significant predictive errors at late-time.

Confirmation of early-time LPI as significant missing physics cannot be assessed due to the lack of resolved, early-time measurements of the shock velocity. However, trajectory QoI observe significant sensitivities to ±50% change in the energy magnitude of the first picket (Fig. 25). Model form errors due to insufficient laser deposition during the first picket may account for $\geq$ 20% of the systematic error in the trajectory QoI. *Validation against early-time laser deposition experiments, such as Cao et al. [7], should be considered to confirm early-time LPI as significant missing physics.*

Non-local Thermal Transport

Local thermal transport models, such as the Spitzer-Harm model, may inadequately predict transport of thermal electrons beyond the mean-free path. This becomes an issue at high laser power and large thermal gradients, where thermal electrons may penetrate as deep as the ablation front and preheat material preceding the shock. Non-local thermal transport models (*e.g.* Schurtz model [35]) overcome this limitation by spreading the Spitzer-Harm current over a larger length scale. Simulations using local thermal transport are often benchmarked against "improved" non-local thermal transport predictions.

As a reference, the non-local thermal transport predictions are compared to the local thermal transport predictions (Fig. 12). Negligible differences between local and non-local models are observed when using the flux limiter ($f = 0.05$). Therefore, it is not an important effect for these simulations. To improve plot clarity, $f = 0.04$, 0.07, and 0.10 are not shown but do not detract from this conclusions.

Nonlinear Laser Plasma Interactions

Many nonlinear LPI contribute to the extra scattering of incident laser beams. Examples include stimulated Brillouin scattering (SBS), stimulated Raman scattering (SRS), and parametric decay instability (PDI) [8]. However, as suggested in the literature [33, 20, 19], CBET has been identified as a dominant source of extra scattering for direct-drive ICF . CBET occurs as reflected and scattered laser rays interact with an incoming beam in the corona. The outgoing light scatters the incoming light via SBS [33].

In simulation, linear CBET models used with non-local heat conduction significantly improve scattered energy predictions (Igumenshchev *et al.* [19]). Insufficient improvements are observed when using non-local heat conduction or linear CBET models alone (Igumenshchev *et al.* [19]). Igumenshchev *et al.* [20], later demonstrated reduced CBET scattering by varying several mechanisms suggested by CBET theory. These mechanisms included beam spot size, laser wavelength variations, and high-Z dopants in the shell.

Igumenshchev *et al.* [19] estimate the incident laser energy lost due to CBET can be as large as 10-20%. Referring to Fig. 7, the comparison error during the primary drive is $e_{P_s} \approx$13-20%ϕ_{P_i}. This suggests a deficet similar to that expected by CBET.

The xRAGE laser package does not have a supported implementation of non-local heat transport with corrections to account for CBET. CBET transport models do exist in current Mazinisin versions implemented in DRACO [21] and are being developed for future versions of the xRAGE laser package. It is worth noting, to date, Mazinisin is the only laser package that has demonstrated CBET predictive capabilities.

3.6.3 Calibration Methods

Currently, the ICF community uses calibration to overcome predicted laser energy deposition deficiencies. Two accepted methods are,

1. **Flux limiter adjustment:**
   The flux limiter is tuned to match critical experimental metrics (*e.g.* bang time, trajectory, or laser absorption).
2. **Laser energy scaling:**
   The flux limiter is fixed at a flux limiter independent value ($f \geq 0.075$) and the incident laser energy scaled to match the absorption energy [9].

Although adjusting the model incident energy input or flux limiter is a ***non-physical calibration that is in conflict with validation****, it is a common method used in the ICF community and by xRAGE users. To assess current modeling techniques used by the community, the strengths, weaknesses, sensitivities, and subtleties of accepted tuning methods will be addressed.*

Thermal Flux Limiter

It is well known that the use of the Spitzer electron thermal conduction model significantly overpredicts laser drive (see Spitzer and Harm [36]. Malone *et al.* [27] suggest using a flux limiter to limit the fluxes of the Spitzer conduction model. Although widely accepted, the flux limiter has little physical significance [20]. Optimal flux limiter values for both ablators range from $0.03 \leq f \leq 0.04$.

However, as noted by Dodd *et al.* [9], with the flux limiter alone, one is often unable to match multiple experimental QoI (*e.g.* bang time, trajectory, or laser absorption). The optimal flux limiter is also extremely sensitive to ablator material, laser intensity and can vary between $0.03 \leq f \leq 0.05$

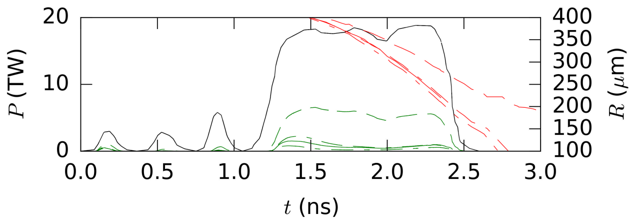

Figure 12: Sensitivity to the flux limiter and identification of the flux limiter independent value (*i.e.* non-local Schurtz model (—) and local Spitzer models with f = 0.03 (——), f = 0.05 (———), and f = 0.15 (——), respectively. Comparison of scattered laser energy (green) and shell trajectory (red). The results are presented for the C ablator shell at high laser power. Incident laser power (black) is shown as a reference. For plot clarity, f = 0.04, 0.07, and 0.10 are not shown.

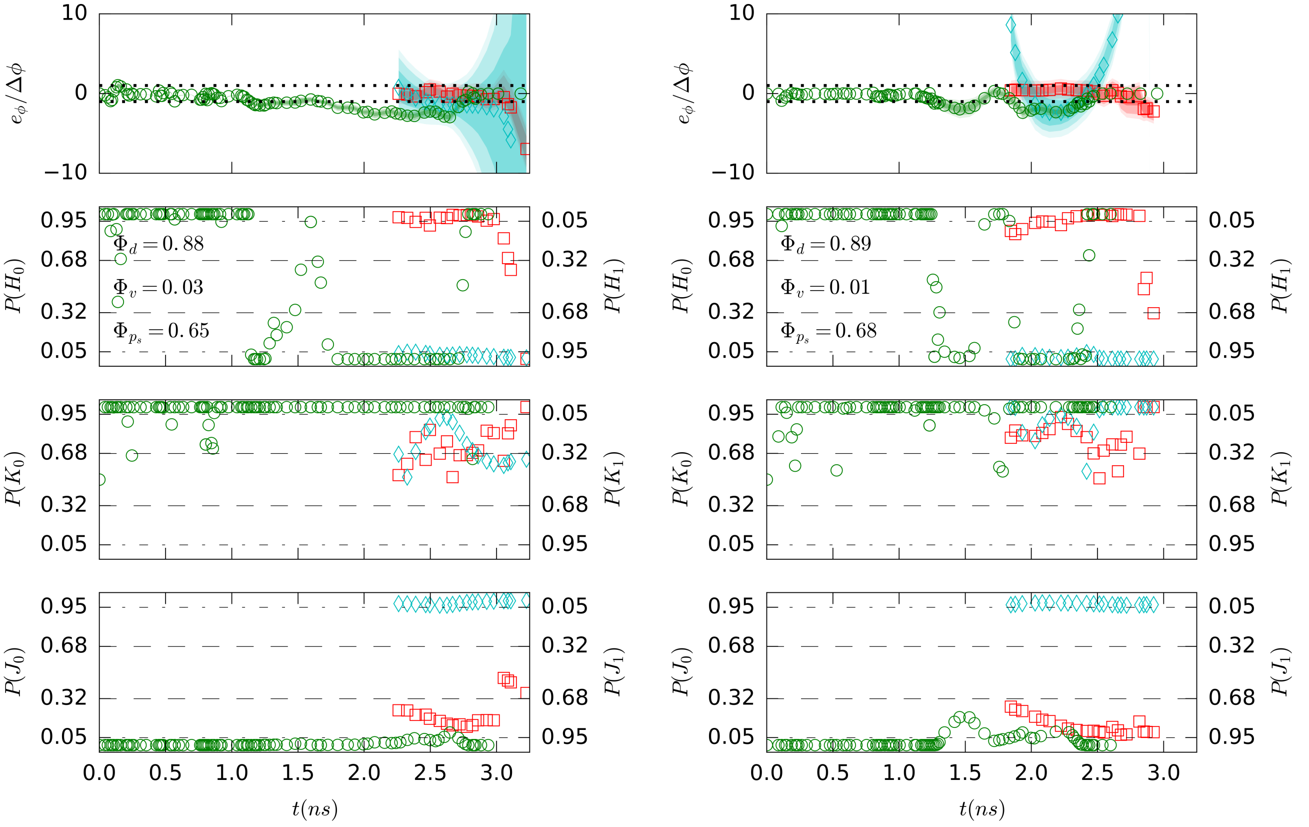

(a) C (l) - Flux Limiting

(b) C (h) - Flux Limiting

Figure 13: Validation assessment of QoI (top) and model error normalized by model requirements (bottom) for the flux limiting case. Comparison of scattered laser energy (green), shell trajectories (red), and shell velocities (cyan) for experimental data (symbols) [29] and xRAGE (lines). Validation uncertainty (*i.e.* 1σ, 2σ, and 3σ confidence) given as shaded regions. Incident laser power (black) is shown as a reference.

The flux limiter can be calibrated independently for each case; however, predictability suffers significantly. Instead, we use the optimal Be (high) flux limiter ($f = 0.035$). This corresponds closely to the optimal flux limiter to predict ablation front trajectories for all cases.

A significant improvement in model confidence is achieved for all QoI (see validation results in Fig. 14). With the exception of the Be (low) case, the ablation front position consistently matches the data. However, a significant systematic error still exists for the Be (low) case.

For the remaining QoI (scattering energy and velocity), a systematic errors exist during the primary drive. However, the shape of the systematic error is inconsistent between ablator materials and laser energies. Once again, the flux limiter is a knob that disregards physics. We have polluted the predictive results for these cases by tuning an unpredictive, physically insignificant quantity. Users should be reluctant to rely on the flux limiter calibration.

The analyst should be aware that the validation uncertainty is similar in magnitude to the comparison error for the trajectory position and velocity. Improvement on the validation assessment requires the analyst to identify and reduce the appropriate uncertainty components.

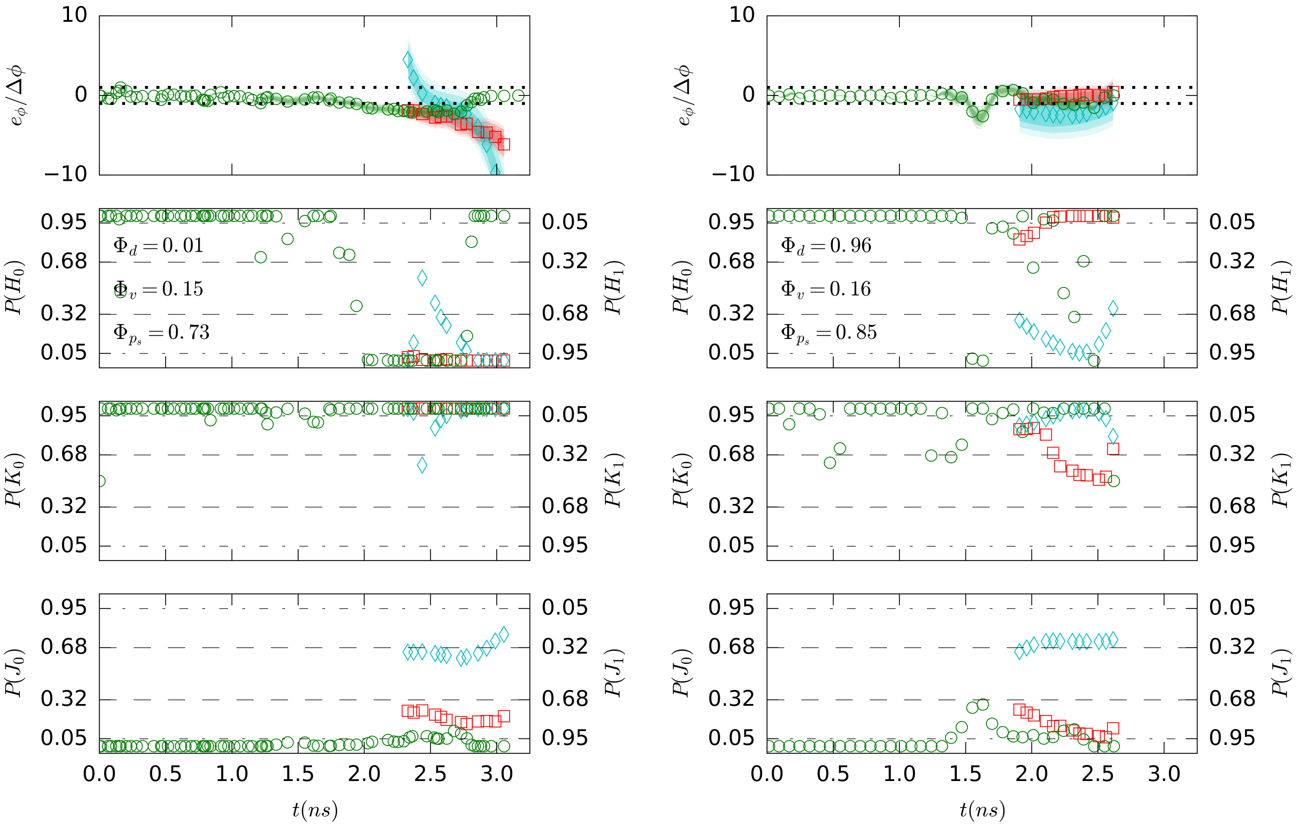

(a) Be (l) - Flux Limiting

(b) Be (h) - Flux Limiting

Figure 14: Validation assessment of QoI (top) and model error normalized by model requirements (bottom) for the flux limiting case. Comparison of scattered laser energy (green), shell trajectories (red), and shell velocities (cyan) for experimental data (symbols) [29] and xRAGE (lines). Validation uncertainty (*i.e.* 1σ, 2σ, and 3σ confidence) given as shaded regions. Incident laser power (black) is shown as a reference.

Incident Laser Scaling

Dodd *et al.* [9] recognized that one can tune the thermal flux limiter to match individual validation metrics, but not all metrics. He suggests an alternative method: scale the incident laser energy to match multiple validation metrics (see Appendix C.1).

Unlike the flux limiter, scaling the incident energy has a physical, although weak, reasoning based on reduced laser absorption due to CBET physics. If CBET is the dominant source of scattered laser energy, perhaps the laser-driven capsule is better simulated by matching the absorbed energy.

Dodd *et al.* [9] observes they are better able to match multiple metrics by scaling incident laser energy at large flux limiter values. At large flux limiters, a flux limiter independent solution regime exists, in which the solution is insensitive to the flux limiter. Our results show the flux limiter in which a flux limiter independent solution occurs is around $f \geq 0.075$.

CBET is strongly dependent on incident laser intensity. QoI predictions for the scaled laser energy calibration (Fig. 16) confirm the likelihood of CBET being the missing physics or model form error. Scaling is determined by the ratio of the experimental to simulation total integrated absorbed energy ($\frac{\phi_{p_{a,exp}}}{\phi_{p_{a,sim}}}$).

For the low incident energy cases, $\frac{\phi_{p_{a,exp}}}{\phi_{p_{a,sim}}} \approx 0.83$, whereas $\frac{\phi_{p_{a,exp}}}{\phi_{p_{a,sim}}} \approx 0.75$ for the high incident energy cases. Note the similar deficit expected by Igumenshchev *et al.* [19] (*i.e.* 10-20%). This indicates the role of the dominant portion of the model form error is to increase the scattered laser light with incident intensity. CBET is known to become more significant as laser intensity increases.

When the incident laser energy is scaled, all QoI consistently match the data during triple picket and primary drive for the Be (high), C (low), and C (high) cases (Fig. 16). Like the flux limiter calibration, a systematic error is still observed in ϕ_{p_s} at very early stages of the primary drive pulse. However, the shape is now consistent between materials and laser energies: the primary drive transition is led by an overshoot, followed by a strong undershoot. *This should increase confidence in the laser scaling method to consistently capture physically-relevant phenomena better than the flux scaling method.*

An additional LPI model form error may still exist, such as an uncharacterized dopplar shifting errors in the diagnostics [8], or temporal response errors from the diagnostic. To better understand this region, we suggest using the wavelength spectra as an additional validation metric in the future.

Calibration Summary

Both calibration methods (*i.e.* flux limiter scaling and laser energy scaling) show significant improvments in matching the experimental data. However, this comes at the cost of predictability. Calibration cannot be performed *a priori* and are completed on a case-by-case basis.

Both methods also indicate reduced energy deposited into the ablator capsule and lend support to CBET being important missing physics. For the laser-energy scaling case, the calibration characteristics are similar to those expected from CBET. For example, experimental evidence suggests a 10-20% scattering enhancement due to CBET. The laser-energy scaling calibration requires the removal of 15-20% incident laser energy to match the data.

3.6.4 Uncertainty Characterization

Experimental Uncertainty

The rigorous characterization of experimental uncertainties by Michel *et al.* [29, 30] is one of the reasons for identifying this experiment as a validation benchmark. The experimental QoI uncertainty is defined as the standard uncertainty. For experimental standard uncertainty magnitudes, the reader is referred to Appendix B and A and Michel *et al.* [29, 30].

Numerical Uncertainty

Numerical uncertainty is often referred to as discretization uncertainty. These simulations use AMR, complicating the use of standard methods to characterize the numerical uncertainty. AMR attempts to minimize discretization

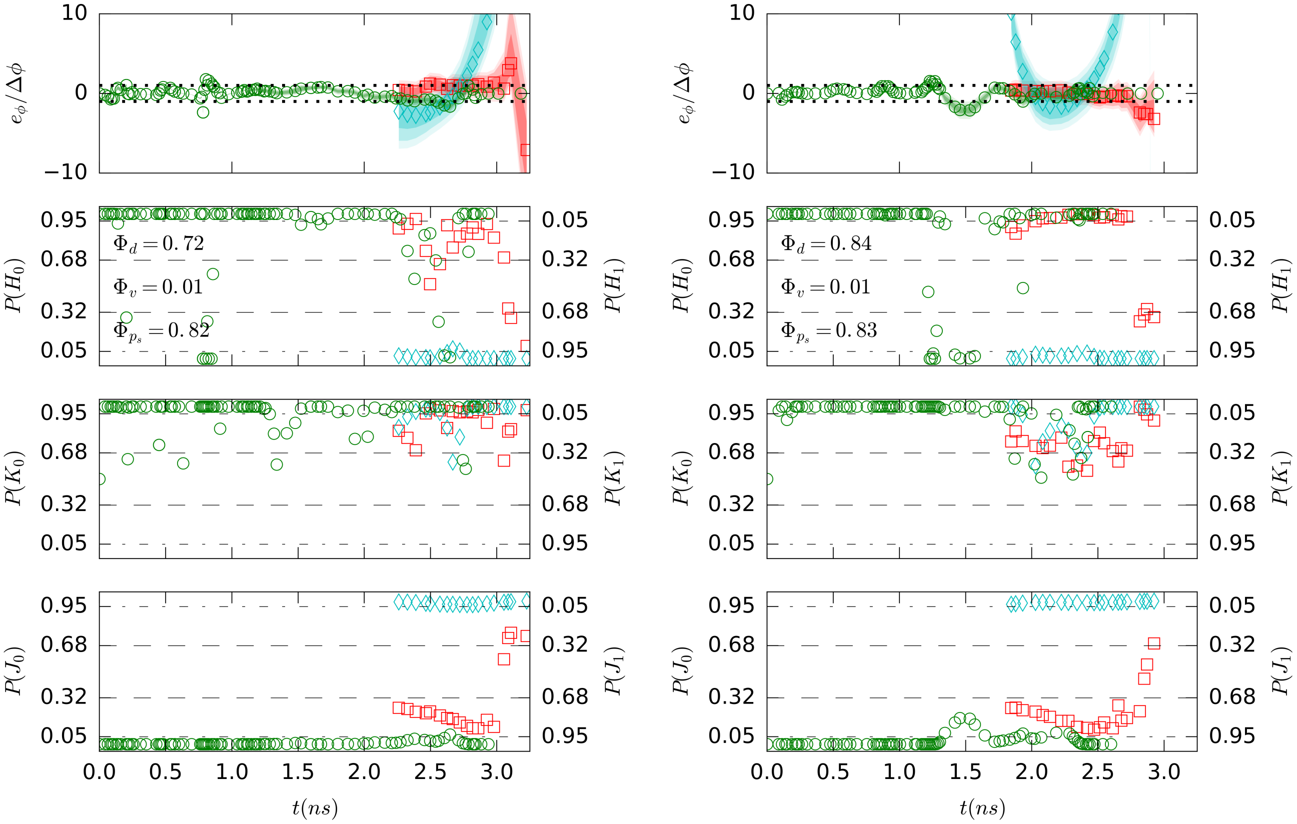

(a) C (l) - Laser Scaling, $\frac{P_{a,exp}}{P+a,sim} \approx 0.83$

(b) C (h) - Laser Scaling, $\frac{P_{a,exp}}{P+a,sim} \approx 0.75$

Figure 15: Validation assessment of QoI (top) and model error normalized by model requirements (bottom) for the laser scaling case. Comparison of scattered laser energy (green), shell trajectories (red), and shell velocities (cyan) for experimental data (symbols) [29] and xRAGE (lines). Validation uncertainty (*i.e.* 1σ, 2σ, and 3σ confidence) given as shaded regions. Incident laser power (black) is shown as a reference.

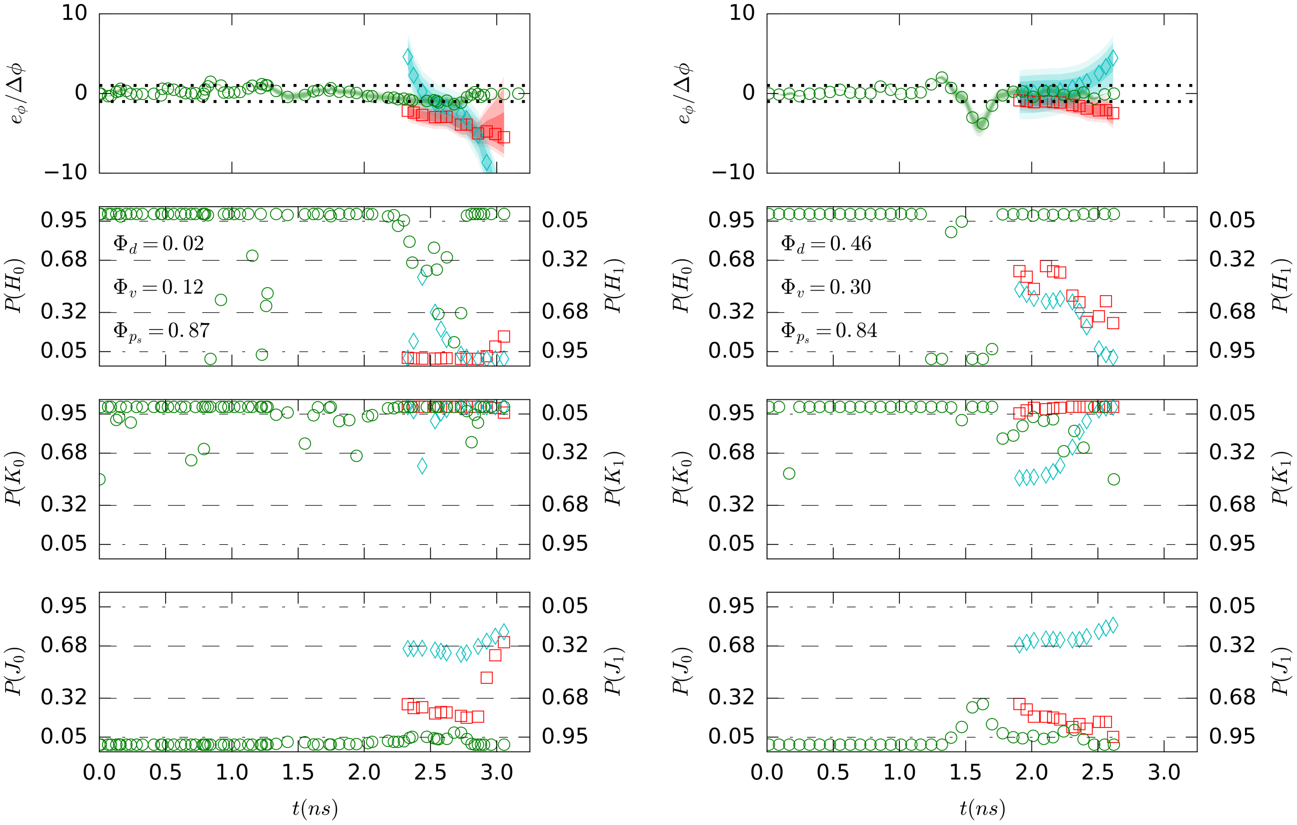

(a) Be (l) - Laser Scaling, $\frac{P_{a,exp}}{P+a,sim} \approx 0.82$

(b) Be (h) - Laser Scaling, $\frac{P_{a,exp}}{P+a,sim} \approx 0.73$

Figure 16: Validation assessment of QoI (top) and model error normalized by model requirements (bottom) for the laser scaling case. Comparison of scattered laser energy (green), shell trajectories (red), and shell velocities (cyan) for experimental data (symbols) [29] and xRAGE (lines). Validation uncertainty (*i.e.* 1σ, 2σ, and 3σ confidence) given as shaded regions. Incident laser power (black) is shown as a reference.

errors by refining the solution grid locally. Refinement is limited by a minimum AMR mesh size defined by the analyst.

Standard methods of assessing u_N require comparison of solution grids which are 1) carefully controlled and 2) uniformly refined. Both are not satisfied when using AMR.

This poses the question, “What should we expect from solution convergence and mesh sensitivity when using AMR?” This is followed by the more important question, “When using AMR, how can we quantify our model numerical uncertainty or our confidence in the model discretization?” The authors believe that these are outstanding questions and will be an active area for future research.

In the absence of a rigorous solution to these questions, we use a method to make an estimate with reasonable confidence of the numerical uncertainty. The method and the “reasonableness” of the confidence is defined operationally in the following.

First, we define a nominal mesh size δx, which is the average initial mesh size, and the minimum AMR cell size δx_{AMR}. We refine the average mesh size and minimum AMR cell size uniformly *i.e.* $h = \overline{\delta x_{nom}/\delta x} = \delta x_{nom,AMR}/\delta x_{AMR}$ =16, 8, 4, 2, 1, 0.5, and 0.25. The AMR grid varies spatially and temporally but cannot be refined beyond δx_{AMR}; mesh refinement is neither sequential or uniform locally.

Next, the solution error is determined as the difference of the predicted QoI from the grid converged solution. The grid converged solution can be estimated via Richardson extrapolated using all refined AMR grids; however, the Richardson extrapolation estimate remains uncertain due to non-monotonic local grid convergence, precision uncertainties at zero-crossings and small errors, and AMR grid variability.

Insigificant differences between solutions are observed at highly-refined AMR grids. Thus, we suggest the finest mesh solution may be used as a surrogate for the grid converged solution with negligible uncertainty. The solution error for each grid is estimated as the difference from the finest mesh *i.e.* $\tilde{e}_{N,\phi} = \phi_{h=16} - \phi_h$. Errors for the scattered laser energy and ablation front position are shown in Fig. 17. Numerical noise from interpolating between grids is removed using a Gaussian filter.

Last, an estimate of the numerical uncertainty for the three coarsest grids is calculated using the grid convergence index ([34]) (shown as the gray shaded region in Fig. 17). A safety factor of $F_s = 1.25$ is applied to all regions with a local convergence rate near $r_\phi \approx 1$; otherwise, a safety factor of $F_s = 3.0$ is used. As confirmation, the standard numerical uncertainty $u_{N,h=1}$ provides nearly complete coverage of the solution error $e_{\phi,h=1}$ for the nominal grid size. As a note, uncertainty estimates using the global deviation method (suggested by Phillips and Roy [32]) overestimate the solution error by an order of magnitude.

The solution convergence is illustrated using the $L1$ norm of the QoI errors (plot inset in Fig. 17). A convergence rate of ≈ 1 is observed for the scattered laser energy, consistent with the expected convergence rate in the presence of a shock. The ablation front position converges at a much slower rate than the laser energies (≈ 0.5). The ablation front convergence rate could be reduced due to metric complexity, contamination from post-processing algorithms, or the presence of a contact discontinuity.

Insight into physics and mesh improvement can be deduced from the numerical uncertainty. Large uncertainties, due to large errors between meshes, exist at the first laser picket and early times of the initial drive pulse. Remember, significant nonlinear effects and LPI exist at these times may be a source of the systematic error. Resolution of nonlinear numerical and physical behavior may require increased mesh refinement.

Input Uncertainty

We can categorize the input uncertainties into two types: fossilized and characterized. Both contribute to the model error.

Our fossilized input uncertainties originate from constituitive models informing the primary model, such as tabular EoS and opacity calculations. Errors from the submodels generating these inputs propagate into simulation QoI. For our simulations, uncertainties from these errors are not fully characterized and difficult to propagate into simulation QoI because they are complex, standardized tables. Thus, we “fossilize” or leave errors of this type in the validation error comparison e_ϕ. Sensitivity studies show our simulations are insensitive to fossilized errors from changes in EoS and opacity tables and these errors contribute negligibly to e_ϕ.

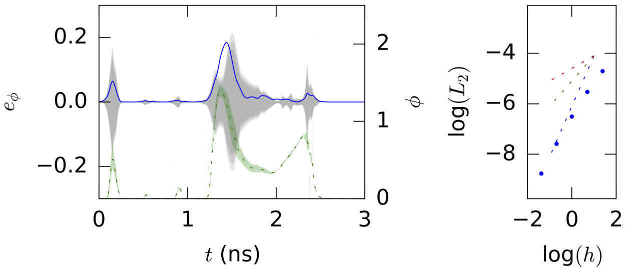

(a) $\phi_{p_s}(TW)$

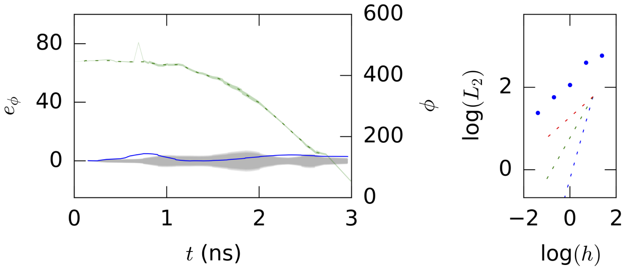

(b) $\phi_r(\mu m)$

Figure 17: Numerical uncertainty assessment of the a) scattered laser energy and b) ablation front position. Estimated numerical error $\tilde{e}_{N,\phi}$ of the nominal grid size (blue) is contained within the GCI-estimated standard numerical uncertainty (shaded gray region). The scattered energy and ablation front QoI with numerical uncertainty (green shaded regions) are shown as a reference. The numerical error $L1$ norm shown on the right with reference convergence rates of one-half, one, and two.

Characterized uncertainties are quantified via ten experimental input parameters, including capsule outer diameter, capsule mass, laser energy, beam radius, and physical properties of the capsule and air (temperatures and densities). Uncertainties on model inputs come from uncertainties characterized by the experimentalists [29, 30].

Using central differencing, the uncertainty contributions from the dominant input parameters are shown in Fig. 18. Uncertainties in the capsule geometry are the dominant uncertainty sources. To reduce input uncertainties, uncertainties in the capsule geometries should be better characterized or reduced. Negligible uncertainty sources, such as the inner and outer gas pressures and densities, are not shown in Fig. 18.

The input parameter uncertainties are propagated into the simulation QoI via latin hypercube sampling (LHS). Input parameter distributions are assumed to be Gaussian with the standard deviation defined as the parameter uncertainty (see Appendix B). Ten sample sets for each input parameter are used to generate a latin hypercube sampling of $n_{LHS} = 100$ cases. The advantages of using LHS instead of central differencing include the ability to capture input parameter correlations, nonlinear physical and numerical responses, and algorithmic discontinuities (*e.g.* limiters).

Simulations are ran for each input parameter sample set derived from LHS. The 5%, 50%, 68%, and 95% percentile response of each QoI are extracted from the LHS simulation set. These characterize the median (50% percentile), standard deviation (68% percentile) and 95% confidence input uncertainty $u_{I_{95\%},\phi}$ for each QoI. The LHS QoI distribution is nearly Gaussian and the standard uncertainty calculated from the 95% confidence uncertainty ($0.5u_{I_{95\%},\phi}$) and the standard deviation are comparable.

Comparison Uncertainty

Combining the input, numerical, and experimental uncertainties into the total validation uncertainty makes the assumption that all simulation QoI are identical to experimental QoI. We argue this is not always appropriate. Experimental and simulation post-processing differences may contaminate the validation comparison error e_ϕ.Important comparison uncertainties arise from complex (*e.g.* synthetic diagnostic processing), common (*e.g.* least-squares curve fitting), and basic (*e.g.* interpolation of simulation results to discrete experimental locations) sources. Quantification of comparison uncertainty is not explicitly addressed in ASME V&V 20 [2].

Comparison uncertainty sources in this validation set include,

1. the post-processing models used to identify the ablation front between experiment and simulation differ slightly. In the experiment, the half-intensity on the inner edge of the self-emission peak is taken as the ablation front location. However, in the simulation, the ablation front is located at the maximum slope of the inner edge of the temperature profile.
2. trajectory derivatives (*i.e.* velocity) of the ablation front are calculated from least-squares curve fits.
3. interpolation of simuation QoI to experimental QoI.

QoI comparison errors from processing can be incorporated into the validation in three ways. First, it can be incorporated into experimental uncertainties $u_{D,\phi}$ by inverting simulation post-processing procedures for experimental results. Second, we can assume the post-processing model is part of the validation model, and, thus, lump the comparison error into the validation comparison error e_ϕ.

The third method suggests the comparison error be a distinct source of characterized uncertainty:

- **Comparison Uncertainty** $u_{C,\phi}$
  Uncertainty from comparing the experimental metric with a simulation metric calculated by differing post-processing methods, (*e.g.* ablation front trajectory processing).

By doing this, an analyst will validate their primary model as opposed to coupled primary and post-processing models.

For now, we lump the comparison error into the validation comparison error e_ϕ. Quantifying and propagating the comparison uncertainty is left for a future discussion.

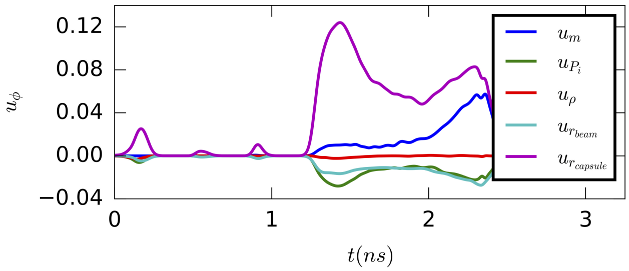

(a) $\phi_{p_s}(TW)$

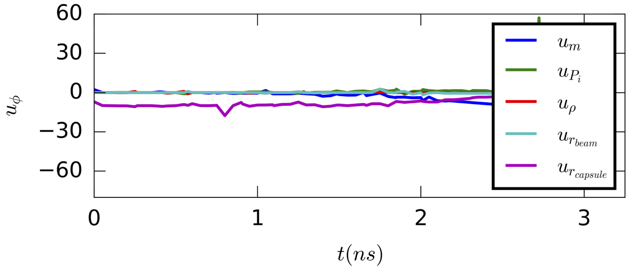

(b) $\phi_r(\mu m)$

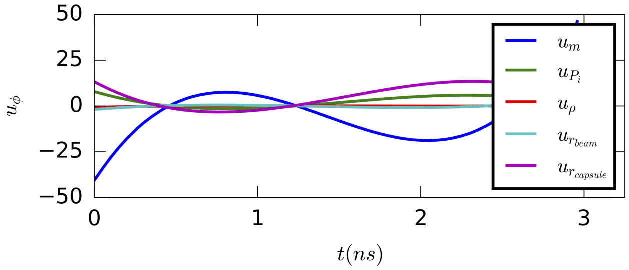

(c) $\phi_v(km/s)$

Figure 18: Contributions of input parameters (*i.e.* mass m_a, incident laser power P_i, density ρ_a, beam radius r_{beam}, and capsule radius r_o) to the total validation uncertainty $u_{V,\phi}$ for the C high case. Input parameters with negligible influence (*e.g.* inner and outer gas pressures and densities) are not shown.

Total Uncertainty Contributions

The validation uncertainty $u_{V,\phi}$ is dominated by experimental uncertainties $u_{D,\phi}$ (Fig. 19). For the laser energy QoI, the experimental uncertainty is usually greater than 95% of the total validation uncertainty. As mentioned earlier, numerical uncertainties begin to be significant at the first laser picket and the initial rise in the drive profile. With the exception of the first laser picket and the initial drive profile, the AMR sufficiently resolves the solution mesh to force numerical uncertainties much smaller than the experimental uncertainties.

The largest uncertainty source for the trajectory QoI is still the experimental uncertainty. However, input uncertainties begin to significantly contribute to the validation uncertainty. This effect can be reduced in two ways: 1) use a better method to fit the ablation front trajectories and 2) reduce the uncertainty on experimentally measured input parameters.

3.6.5 Evaluation Summary

In summary, the validation evaluation indicates the dominant source of the unacceptable model is due to a systematic error. The error is unlikely to be due to experimental sources, such as unknown facility issues and diagnostic bias. Several missing physics in the model have been suggested. Numerical discretization errors may impact some of the missing physics but were demonstrated to be too small to be the dominant systematic error.

Sensitivity studies and calibration methods both indicate a strong correlation between the systematic error and scattered laser light. Similar symptoms are expected from CBET. We suggest cross-beam energy transfer is the offending missing physics; however, validation evidence does not preclude other nonlinear laser plasma instabilities or physics not considered within this work.

Further validation evidence is required to confirm CBET as the missing physics. Additional diagnostics, such as measurement of the energy spectrum of scattered wavelengths, and CBET-sensitive experiments should be pursued to provide additional CBET evidence.

With the ablation front velocity as the exception, validation uncertainties are sufficiently small to perform an unambiguous validation. Sources of large experimental uncertainties in the ablation front velocity should be assessed to reduce ambiguity.

3.7 Validation Recommendations

From the previous validation assessment, several recommendations are suggested regarding model-usage and prioritization of resource allocation:

Model Usage

- The current xRAGE/Mazinisin implementation has a model form error. Likely model form errors, ranked by priority, include:
    1. unmodeled nonlinear LPI, such as cross-beam energy transfer (CBET),
    2. insufficient laser deposition during the first laser picket,
    3. neglect of NLTE opacity.
- The ablation front velocity validation is ambiguous due to large experimental uncertainties.
- Common CBET mitigation techniques improve model accuracy.
    - However, these are based on weak physics bases and are calibrated at the expense of predictability.
    - The laser-scaling calibration is more physically-based and improves QoI across the board
- The model is insensitive to many modeling choices.
    - The model agrees with non-local thermal conduction with a flux limiter 0.03.

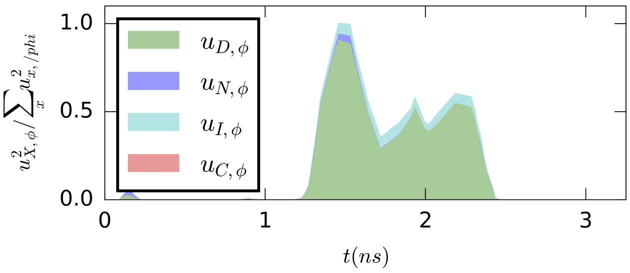

(a) $\phi_{p_s}(TW)$

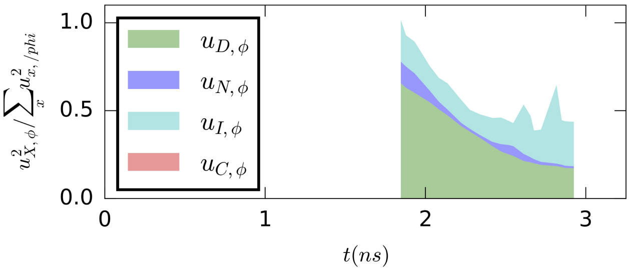

(b) $\phi_r(\mu m)$

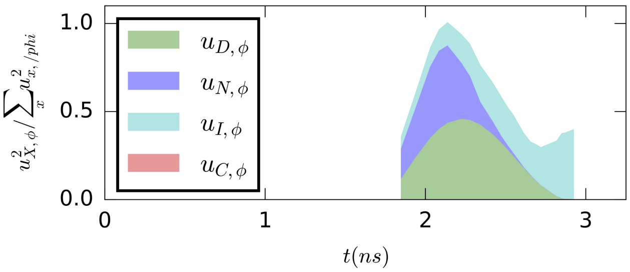

(c) $\phi_v(km/s)$

Figure 19: Normalized contributions of uncertainty components to the total validation uncertainty $u_{V,\phi}$ for the C high case.

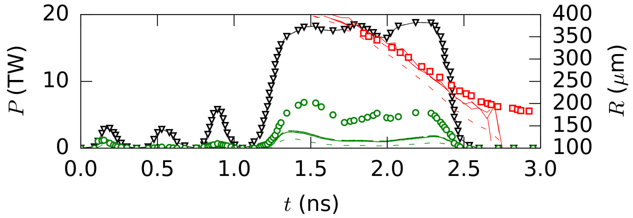

Figure 20: Comparison of 1d and 2d simulation and experimental QoI. Comparison of scattered laser light (green) and shell trajectories (red) for experimental data (symbols) [29] and xRAGE (lines). Simulations are given as dashed lines (1d) and solid lines (2d). Incident laser power (black) is shown as a reference.

  - The model is insensitive to partial ionization, Sesame EOS, and NLTE.

Resource Allocation

- Include CBET capabilities in the xRAGE laser package (Mazinisin).
- Supplement HEDP-VS with experiments that address
  - CBET sensitivity experiments
  - LPI experiments during the first picket

4 Current and Future Work Addressing the Michel2013 Validation Recommendations

Given the evaluation and validation recommendations learned in Section 3, we have begun to pursue new validation evidence. First, the xRAGE laser package has been updated to include CBET predictive capabilities. This new package will be assessed with the Michel2013 validation experiment in FY2020. Additionally, new questions regarding the use of CBET will be evaluated, such as

1. What sensitivities and knobs exist and must be constrained for predictive use of the CBET model?
2. Does the CBET model improve accuracy, confidence, acceptability, and predictiveness of xRAGE under the given experimental conditions?
3. In what regimes should we be careful when applying the CBET model?

In addition to assessing the new CBET-capable xRAGE laser package, we have also begun adding new experiments into the HEDP-VS. These are outlined in the following sections.

4.1 2d Michel2013

We first consider differences between the nominal model in 1d verus 2d. The 2d Michel2013 model shows some improvement in predicting scattered laser energy (see Fig. 20). The higher-fidelity 2d model accounts for oblique scattering from the curved capsule surface and increases the scattered light by ≈5% of the incident laser energy. Referring back to Section 3.6.3, an increase of scattered laser light brings the simulation in better agreement with scattering estimates from CBET experiments (*i.e.* 10-20%).

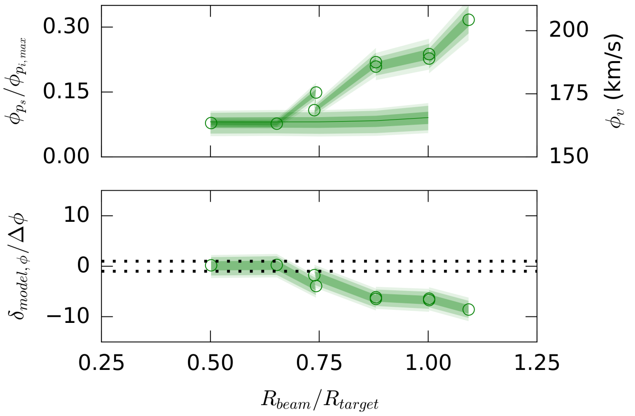

Figure 21: Validation assessment of QoI (top) and model accuracy normalized by model requirements (bottom). Comparison of scattered laser energy percentage for experimental data (symbols) [29] and xRAGE (lines). Validation uncertainty (*i.e.* 1σ, 2σ, and 3σ confidence) given as shaded regions.

As expected, the decrease in predicted absorbed laser energy results in reduced acceleration and better agreement of the ablation front QoI. However, the ablation front trajectory is still underpredicted, particularly, at late times. Further investigation is required to better understand the differences between 1d and 2d xRAGE simulations of Michel2013.

4.2 Froula2012

CBET is caused by the interaction of refracted light interacting with incoming beams and redirecting laser energy through stimulated Brillioun scattering. With that in mind, by reducing the beam radius with respect to the capsule radius, refracted light will be reduced. Froula2012 [12] is an experiment designed to investigate the sensitivity of capsule implosion to CBET by studying implosions for various beam to capsule size ratios ($\frac{R_{beam}}{R_{capsule}}$). Simulations in 1d xRAGE are shown in Fig. 21 and show good agreement at small $\frac{R_{beam}}{R_{capsule}}$ when CBET has little impact.

Applying the validation assessment workflow, $\frac{R_{beam}}{R_{capsule}} \leq 0.75$ agrees well and has a low probability of a systematic error (Fig. 22). For large ratios, the model is unacceptable and has high probability of a systematic error. Once again, we believe this is due to CBET.

In addition to a systematic error, Froula2012 experiments were not as well characterized as Michel2013. Consequently, there is increased probability of ambiguity, even with the integrated QoI measured in Froula2012.

4.3 Hu2008

As shown earlier, there is a strong coupling between absorbed laser energy and material motion. The complex, coupled processes of converting absorbed laser energy into material motion or kinetic energy are also of interest. In particular, we are interested in how well xRAGE predicts the material motion when not impacted by LPI, such as CBET.

To study this, we have begun validation of planar ablation experiments at Omega (see Hu *et al.* [18]). In the Hu2008 planar ablation experiments, a planar CH foil is driven by high energy lasers. Several cases at various laser energies are investigated and shown in Fig. 23. As the laser energy is deposited onto the surface, the opposing foil surface is driven at high velocities and measured using radiography. Preliminary 1d and 2d simulations show good agreement at early times, but begin to deviate at late times.

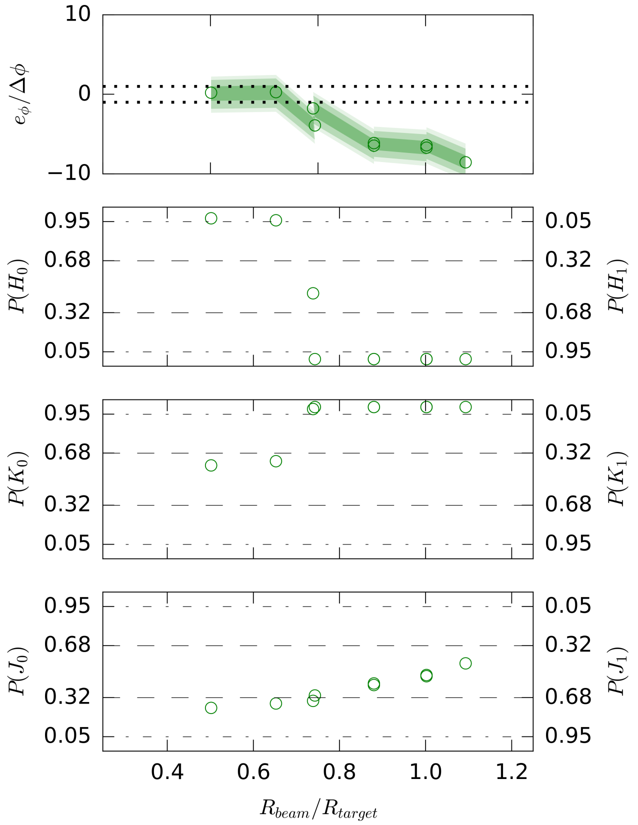

Figure 22: Validation assessment metrics for Froula2012: from top to bottom, model accuracy normalized by model requirements, model acceptability, probability of a systematic error, and probability of ambiguity. Comparison of scattered laser energy percentage for experimental data (symbols) [12] and xRAGE (lines). Validation uncertainty (*i.e.* 1σ, 2σ, and 3σ confidence) given as shaded regions.

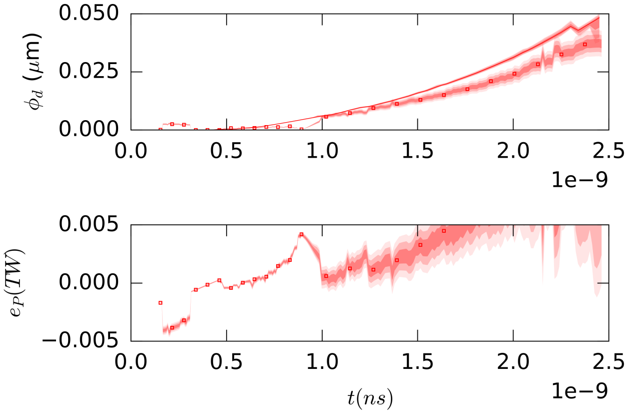

(a) $\phi_{p_a}(TW)$

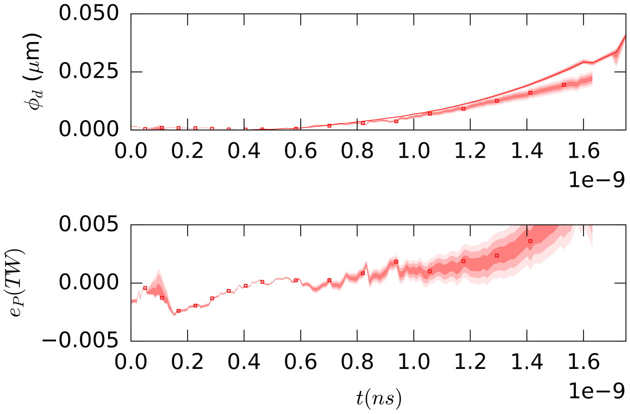

(b) $\phi_{p_s}(TW)$

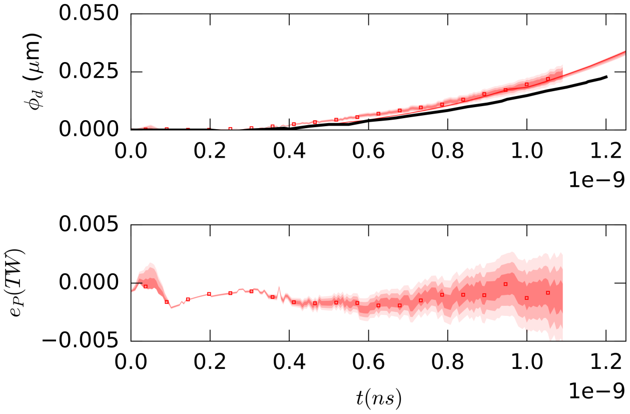

(c) $\phi_r(\mu m)$

Figure 23: Validation assessment QoI for Hu2008: validation comparison (top) and model accuracy (bottom). Comparison of accelerated foil position for experimental data (symbols) [29] and xRAGE (lines). Validation uncertainty (*i.e.* 1σ, 2σ, and 3σ confidence) given as shaded regions.

5 Conclusion

In this paper we quantitatively assess the current implementation of the laser-package in xRAGE. Assessment of the laser package is currently limited to single-shell, laser-driven, direct-drive experiments from the Omega laser facility (see Michel *et al.* [30]).

The validation assessment is based on the validation assessment workflow [38], in which, model accuracy, confidence, and acceptability are rigorously quantified. The code is also rigorously evaluated based on the intended uses of the model, model usage, and prioritization of resource allocation. Based on the results of this assessment, several recommendations are made for model usage and resource allocation:

Model Usage

- The current xRAGE/Mazinisin implementation has a model form error. Likely model form errors, ranked by priority, include:
    1. unmodeled nonlinear LPI, such as cross-beam energy transfer (CBET),
    2. insufficient laser deposition during the first laser picket,
    3. neglect of NLTE opacity.
- The ablation front velocity validation is ambiguous due to large experimental uncertainties.
- Common CBET mitigation techniques improve model accuracy, but limit predictability.
- The model is insensitive to many modeling choices.

Resource Allocation

- Include CBET capabilities in the xRAGE laser package (Mazinisin).
- Supplement HEDP-VS with experiments that address
    - CBET sensitivity experiments
    - LPI experiments during the first picket

Qualitatively, the validation assessment indicates the existance of a model form error. Both the validation assessment and calibration suggest CBET and LPI to be the likely missing physics. Confirmation of this hypothesis should be addressed by the inclusion of validation experiments that probe CBET physics. Viable experiments to be included in the HEDP-VS are variable CBET sensitivity implosions [20, 12, 31], early-time first picket LPI implosions [14], and foil ablation [18]. Preliminary validation on a subset of new experiments was demonstrated and confirm earlier findings.

The reader is reminded that this validation assessment and calibration assessment pertains only to this set of problems. Models may be more or less predictive of other important quantities for ICF, *e.g.* bang time, etc. Assessment of additional validation QoI, such as laser scattering spectra and bang time, is suggested for better understanding of CBET and ICF predictive capabilities.

Validation assessments addressing the recommendations from the Michel2013 validation are outlined. FY2020 directions include assessing 2d modeling improvements and CBET predictive capability. Additional experiments (*e.g.* Froula2012 and Hu2008) will be further assessed in FY2020.

Acknowledgements

This work was supported by the U.S. Department of Energy through the Los Alamos National Laboratory. Los Alamos National Laboratory is operated by Triad National Security, LLC, for the National Nuclear Security Administration of U.S. Department of Energy (Contract No. 89233218CNA000001).

References

[1] Guide for verification and validation in computational solid mechanics. Technical report, ASME, 2006. ASME V&V 10-2006.

[2] Standard for verification and validation in computational fluid dynamics and heat transfer. Technical report, ASME, 2009. ASME V&V 20-2009.

[3] S. Atzeni, J. Meyer-Ter-Vehn, and J. Meyer-ter Vehn. *The Physics of Inertial Fusion: BeamPlasma Interaction, Hydrodynamics, Hot Dense Matter*, volume 125. Oxford University Press on Demand, 2004.

[4] P. A. Bradley, J. A. Cobble, I. L. Tregillis, M. J. Schmitt, K. D. Obrey, V. Glebov, S. H. Batha, G. R. Magelssen, J. R. Fincke, S. C. Hsu, N. S. Krasheninnikova, T. J. Murphy, and F. J. Wysocki. Role of shocks and mix caused by capsule defects. *Physics of Plasmas*, 19(9):092703, 2012.

[5] P. A. Bradley, P. H. Denne, B. M. Haines, P. W. McKenty, T. Collins, and D. Keller. Update on RAGE code laser simulations. 2015 Nuclear Explosives Design Physics Conference, 2015. (LA-UR-15-24908).

[6] P. A. Bradley, M. L. Hall, P. W. McKenty, T. Collins, and D. Keller. Testing a new ASC code laser package. 2014 Nuclear Explosives Code Developer's Conference, 2014. (LA-UR-15-20796).

[7] D. Cao, G. Moses, and J. Delettrez. Improved non-local electron thermal transport model for two-dimensional radiation hydrodynamics simulations. *Physics of Plasmas*, 22(8):082308, 2015.

[8] R. Craxton, K. Anderson, T. Boehly, V. Goncharov, D. Harding, J. Knauer, R. McCrory, P. McKenty, D. Meyerhofer, J. Myatt, et al. Direct-drive inertial confinement fusion: A review. *Physics of Plasmas*, 22(11):110501, 2015.

[9] E. S. Dodd, J. F. Benage, G. A. Kyrala, D. C. Wilson, F. J. Wysocki, W. Seka, V. Y. Glebov, C. Stoeckl, and J. A. Frenje. The effects of laser absorption on direct-drive capsule experiments at omega. *Phys. Plasmas*, 19, 2012.

[10] Eularian Applications Code Team. xRage users manual. Technical report, Los Alamos National Laboratory, 2017. Code Version 1.170710, Last Revised: Sept. 7, 2017. LA-CP-11-00643.

[11] L. H. Frey, W. Even, D. J. Whalen, C. L. Fryer, A. L. Hungerford, C. J. Fontes, and J. Colgan. The los alamos supernova light-curve project: Computational methods. *The Astrophysical Journal Supplement Series*, 204(2):16, 2013.

[12] D. H. Froula and *et. al.* Increased hydrodynamic efficiency by reducing cross-beam energy transfer in direct-drive implosion experiments. *PRL*, 108, 2012.

[13] M. Gittings, R. Weaver, M. Clover, T. Betlach, N. Byrne, R. Coker, E. Dendy, R. Hueckstaedt, K. New, W. R. Oakes, D. Ranta, and R. Stefan. The RAGE radiation-hydrodynamic code. *Computational Science and Discovery*, 1(1):015005, Oct. 2008.

[14] S. Glenzer, W. Rozmus, B. MacGowan, K. Estabrook, J. De Groot, G. Zimmerman, H. Baldis, J. Harte, R. Lee, E. Williams, et al. Thomson scattering from high-z laser-produced plasmas. *Physical Review Letters*, 82(1):97, 1999.

[15] V. Goncharov, P. McKenty, S. Skupsky, R. Betti, R. McCrory, and C. Cherfils-Clérouin. Modeling hydrodynamic instabilities in inertial confinement fusion targets. *Physics of Plasmas*, 7(12):5118–5139, 2000.

[16] B. M. Haines. personal communication.

[17] B. M. Haines, G. P. Grim, J. R. Fincke, R. C. Shah, C. J. Forrest, K. Silverstein, F. J. Marshall, M. Boswell, M. M. Fowler, R. A. Gore, et al. Detailed high-resolution three-dimensional simulations of omega separated reactants inertial confinement fusion experiments. *Physics of Plasmas*, 23(072709), 2016.

[18] S. X. Hu, V. A. Smalyuk, V. N. Goncharov, S. Skupsky, T. C. Sangster, D. D. Myerhofer, and D. Shvartz. Validation of thermal transport modeling with direct-drive, planar-foil acceleration experiments at OMEGA. *Physical Review Letters*, 101(055002), 2008.

[19] I. Igumenshchev, D. Edgell, V. Goncharov, J. Delettrez, A. Maximov, J. Myatt, W. Seka, A. Shvydky, S. Skupsky, and C. Stoeckl. Crossed-beam energy transfer in implosion experiments on omega. *Physics of Plasmas*, 17(12):122708, 2010.

[20] I. V. Igumneshchev and *et. al.* Crossed-beam energy transfer in direct-drive implosions. *Phys. Plasmas*, 19, 2012.

[21] D. Keller, T. J. B. Collins, J. A. Delettrez, P. W. McKenty, P. B. Radha, R. P. J. Town, B. Whitney, and G. A. Moses. Draco—a new multidimensional hydrocode. In *APS Division of Plasma Physics Meeting Abstracts*, 1999.

[22] S. H. Langer, I. Karlin, and M. M. Marinak. Performance characteristics of hydra–a multi-physics simulation code from LLNL. In *International Conference on High Performance Computing for Computational Science*, pages 173–181. Springer, 2014.

[23] D. S. Lemons. *An introduction to stochastic processes in physics*. The Johns Hopkins University Press, Baltimore, MD, 2002.

[24] J. D. Lindl, P. Amendt, R. L. Berger, S. G. Gendinning, S. H. Glenzer, S. W. Haan, R. L. Kauffman, O. L. Otto, and L. J. Suter. The physics basis for ignition using indirect-drive targets on the National Ignition Facility. *Physics of Plasmas*, 11(2):339–491, 2004.

[25] S. P. Lyon and J. D. Johnson. SESAME: The Los Alamos National Laboratory equation of state database. Technical report, LANL, 1992. LA-UR-92-3407.

[26] N. Magee, J. Abdallah Jr, R. Clark, J. Cohen, L. Collins, G. Csanak, C. Fontes, A. Gauger, J. Keady, D. Kilcrease, et al. Atomic structure calculations and new Los Alamos astrophysical opacities. In *Astrophysical Applications of Powerful New Databases*, volume 78, page 51, 1995.

[27] R. C. Malone, R. L. McCrory, and R. L. Morse. Indications of strongly flux-limited electron thermal conduction in laser-target experiments. *Physical Review Letters*, 34, 1975.

[28] J. A. Marozas. Wavelength detuning cross-beam energy transfer mitigation scheme for direct-drive modeling and evidence form National Ignition Facility implosions. APS Division of Plasma Physics, October 2017.

[29] D. T. Michel, R. S. Craxton, A. K. Davis, R. Epstein, V. Y. Glebov, V. N. Goncharov, S. X. Hu, I. V. Igumenshchev, D. D. Myerhofer, P. B. Radha, T. C. Sangster, W. Seka, C. Stoeckl, and D. H. Froula. Implosion dynamics in direct-drive experiments. *Plasma Phys. Control Fusion*, 57, 2015.

[30] D. T. Michel, V. N. Goncharov, I. V. Igumenshchev, R. Epstein, and D. H. Froula. Demonstration of the improved rocket efficiency in direct-drive implosions using different ablator materials. *Physical Review Letters*, 111, 2013.

[31] K. Molvig, M. J. Schmitt, B. Albright, E. Dodd, N. Hoffman, G. McCall, and S. Ramsey. Low fuel convergence path to direct-drive fusion ignition. *Physical Review Letters*, 116(25):255003, 2016.

[32] T. S. Phillips and C. J. Roy. A new extrapolation-based uncertainty estimator for computational fluid dynamics. *Journal of Verification, Validation and Uncertainty Quantification*, 1(4):041006, 2016.

[33] C. Randall, J. R. Albritton, and J. Thomson. Theory and simulation of stimulated brillouin scatter excited by nonabsorbed light in laser fusion systems. *The Physics of Fluids*, 24(8):1474–1484, 1981.

[34] P. J. Roache. Quantification of uncertainty in computational fluid dynamics. *Annual Review of Fluid Mechanics*, 29(1):123–160, 1997.

[35] G. Schurtz, P. D. Nicolai, and M. Busquet. A nonlocal electron conduction model for multidimensional radiation hydrodynamics codes. *Physics of plasmas*, 7(10):4238–4249, 2000.

[36] L. Spitzer and R. Härm. Transport phenomena in a completely ionized gas. *Phys. Rev.*, 89:977–981, Mar 1953.

[37] I. Tregillis, B. M. Wilson, and A. Koskelo. Comparison of metrics for validation assessment. *J. VV&UQ, in preparation*, pages 1 – 15, 2019.

[38] B. M. Wilson and A. Koskelo. Assessment of model onfidence of a laser source model in xRAGE using Omega direct-drive implosion experiments. *J. VV&UQ*, pages 1 – 15, 2018.

[39] B. M. Wilson and A. Koskelo. Validation assessment of model acceptability of a laser source model in xRAGE using Omega direct-drive implosion experiments. *J. VV&UQ, in preparation*, pages 1 – 15, 2019.

[40] B. M. Wilson and A. Koskelo. A validation assessment workflow for the development of a comprehensive validation. *J. VV&UQ, in preparation*, pages 1 – 15, 2019.

[41] B. M. Wilson and A. Koskelo. Validation evaluation ssessment of a laser source model in xRAGE using Omega direct-drive implosion experiments. *J. VV&UQ, in preparation*, 3(4):041003, 2019.

[42] B. M. Wilson, A. Koskelo, B. M. Haines, and T. R. Dhakal. Assessing xRage predictive capability using the high-energy density physics validation suite. 48th Annual Anomalous Absorption Conference, 2018.

A Appendix A: Diagnostic Uncertainties

Several diagnostics capture the laser drive physics QoI - see Table 1. The incident laser power P_i is measured upstream of the target interaction during drive. The total scattered laser energy is measured using time-integrated calorimeters. Temporally-resolved, relative scattered spectra are also captured using a high-dynamic range (HDR) streak camera multiplexed into a spectrometer.

Calorimeter measurements are used to scale relative energy measurements from the streak camera to the total scattered energy giving temporally-resolved scattered power P_s (see Fig. 3). The triple picket pulse at $t \approx 0.3$, 0.6, and 0.9ns followed by a long step pulse is observed. A significant portion ($\approx 30\%$) of the incident laser energy is scattered through linear and nonlinear processes. The absorbed laser power P_a by the capsule is calculated as the difference of the incident and scattered laser power.

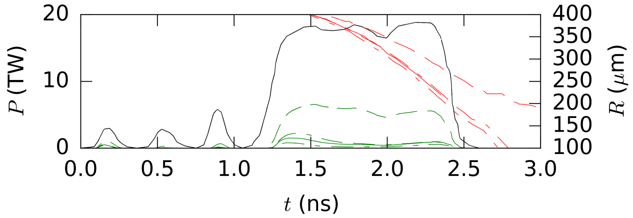

(a) C (h)

Figure 24: Sensitivity to the flux limiter and identification of the flux limiter independent value (*i.e.* non-local Schurtz model (—) and local Spitzer models with $f = 0.03$ (−−), $f = 0.04$ (−−·), $f = 0.05$ (−·), $f = 0.1$ (− (··), and $f = 0.15$(−··), respectively. Comparison of laser power (black), scattered light (green), absorbed light (blue) and shell trajectories (red). The results are presented for the C ablator shell at high laser power. Incident laser power (black) is shown as a reference.

B Appendix B: Nominal Experimental Values and Uncertainties

The nominal values and uncertainty on simulation inputs are given in Table 2. These inputs and ranges are given to the simulation and latin-hypercube sampling techniques for analysis.

C Model Sensitivities

C.1 Flux Limiter Sensitivity

The sensitivity to flux limiter values are shown in Fig. 24. The simulation is extremely sensitive to changes in the flux limiter. Optimal flux limiter values range from $0.3 \leq f \leq 0.4$. However, the flux limiter that agrees best with the non-local thermal conduction model ranges from $0.05 \leq f \leq 0.6$.

The solution begins to be insenstive to the flux limiter around $f \approx 0.075$. In this paper, this is designated as the flux limiter independent regime.

C.2 First Picket Energy Sensitivity

Triple picket pulse profiles are inherently difficult to predict due to LPI effects being on the same order as the first picket energy. Modeling and prediction errors from the first picket will propagate into important late-time QoI. The sensitivity to first picket energy is evaluated by varying the first picket incident energy by $\pm 0.5\phi_{p_{i,t\leq 0.3ns}}$ (see Fig. 25).

The absorbed and scattered laser energies are insensitive to the first picket energy. However, variations in the first picket energy place the capsule on a different hugoniot and alter the trajectory QoI. The first picket energy sensitivity is of similar significance as the flux limiter sensitivity.

C.3 Calculation Control Sensitivity

Simulation sensitivity to calculation control parameters are considered. Simulation results are insensitive to the calculation setup (*e.g.* Δt and number of processors) - Fig 26-27.

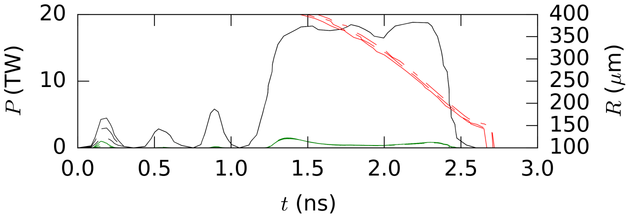

(a) C (h)

Figure 25: Sensitivity to the laser energy deposited during the first laser picket (*i.e.* $1.5P_{i,t\leq 0.3}$ (—), P_i (– –), and $0.5P_{i,t\leq 0.3}$ (– – ·), respectively. Comparison of laser power (black), scattered light (green), absorbed light (blue) and shell trajectories (red). The results are presented for the C ablator shell at high laser power. Incident laser power (black) is shown as a reference.

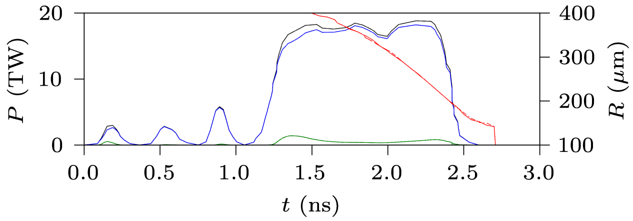

(a) C (h)

Figure 26: Sensitivity to the number of processors (*i.e.* 8 (—), 12 (– –), 16 (– – ·), and 32 (– ·) respectively. Comparison of laser power (black), scattered light (green), absorbed light (blue) and shell trajectories (red). The results are presented for the C ablator shell at high laser power. Incident laser power (black) is shown as a reference.

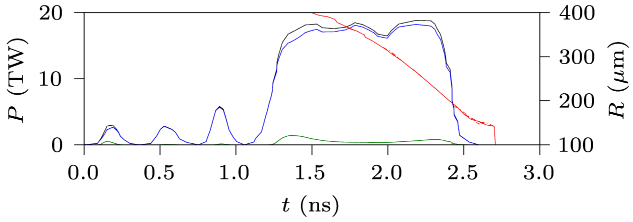

(a) C (h)

Figure 27: Sensitivity to the initial Δt (*i.e.* 1.0×10^{-17} (—), 2.0×10^{-17}12 (– –), 4.0×10^{-17}16 (– – ·), and 8.0×10^{-17} (– ·) respectively. Comparison of laser power (black), scattered light (green), absorbed light (blue) and shell trajectories (red). The results are presented for the C ablator shell at high laser power. Incident laser power (black) is shown as a reference.

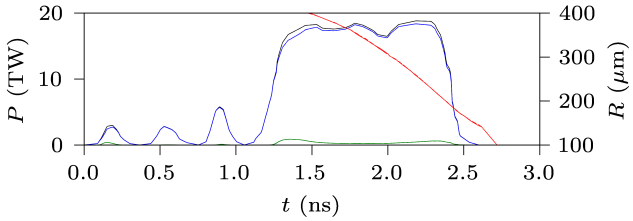

(a) C (h)

Figure 28: Sensitivity to the number of multigroups bins for the opacity calculations (n =60 (—), 100 (−−), and 150 (−− ·)). Comparison of laser power (black), scattered light (green), absorbed light (blue) and shell trajectories (red) for experimental data (symbols) [29] and xRAGE (solid lines). The results are presented for the C ablator shell at high laser power. Incident laser power (black) is shown as a reference.

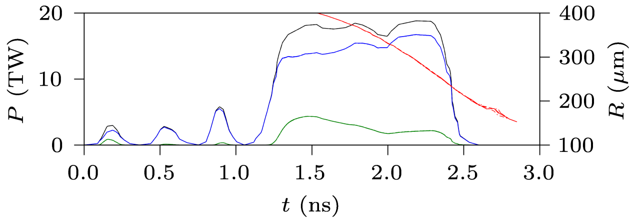

(a) C (h)

Figure 29: Sensitivity to the partial ionization model (*i.e.* full-ionization (—), Saha with number density mix (−−), Thomas-Fermi with electron density mix (−− ·), Thomas-Fermi with number density mix (− ·), and Thomas-Fermi with Zimmerman mix (· ·), respectively. Comparison of laser power (black), scattered light (green), absorbed light (blue) and shell trajectories (red). The results are presented for the C ablator shell at high laser power. Incident laser power (black) is shown as a reference.

C.4 Opacity Sensitivity

Opacities were calculated assuming local thermal equilibrium using TOPS for $n = 60$ multigroup bins defining the photon energy spectrum. Assuming the uncertainty in TOPS calculations for each material is negligible, the model sensitivity is limited to the resolution of the opacity spectrum. This assumption introduces a new fossilized uncertainty that arises from basic physics validation of TOPS.

The number of multigroup bins was varied between $60 \leq n \leq 200$ and results are shown in Fig. 28. The model solution is converged at $n = 60$ multigroups and is insensitive to LTE opacity. The next step is to investigate sensitivity to NLTE.

C.5 Ionization Sensitivity

Sensitivities to other ionization models (*e.g.* Thomas-Fermi, Saha, full ionization) were investigated (Fig. 29). The Saha model with number density mix and the Thomal-Fermi model with three mix definitions were turned on: number density mix, electron density mix, and Zimmerman mix. Mix definitions define methods to combine individual isotopes within a material. As a reference, the full ionization model is also compared.

All simulation metrics are insensitive to the partial ionization model and mix definition.

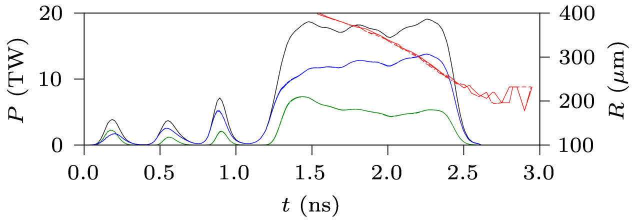

(a) C (h)

Figure 30: Sensitivity to the CH Sesame EoS table (*i.e.* Sesame 7590 (—), Sesame 7591 (−−), Sesame 7592 (−−·), and Sesame 7593 (−·), respectively. Comparison of laser power (black), scattered light (green), absorbed light (blue) and shell trajectories (red). The results are presented for the C ablator shell at high laser power. Incident laser power (black) is shown as a reference.

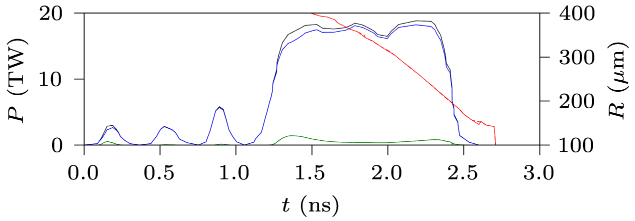

(a) C (h)

Figure 31: Sensitivity to the capsule fill gas (*i.e.* CO_2 (—) and air (−−), respectively. Comparison of laser power (black), scattered light (green), absorbed light (blue) and shell trajectories (red). The results are presented for the C ablator shell at high laser power, respectively. Incident laser power (black) is shown as a reference.

C.6 CH Sesame Table Sensitivity

Several Sesame EoS tables exist for CH with the most current being Sesame 7593. A study of the simulation sensitivity to Sesame definitions is shown in Fig. 30. Although negligible differences are observed, it is recommended that Sesame 7590 be used in future simulations.

C.7 Capsule Fill Gas Sensitivity

Although the capsule is under vacuum, we assume some residual gas exists in the capsule interior. The initial (pre-evacuation) gas composition and gas fill pressure is unknown. The uncertainty from the gas fill pressure was quantified in the input uncertainty. However, the gas composition could affect EoS, hydrodynamics, and opacities.

The QoI in this validation study are insensitive to two gas compositions: air and CO_2 (Fig. 31). The insensitivity is due to the insignificant volume of gas in the capsule interior. If the experiments were conducted at higher capsule pressures, the QoI response to gas composition may no longer be negligible.

Table 1: Experimental metrics and uncertainty [30]

Validation Metric	Uncertainty
Incident Calorimeters	
Incident Laser Power (P_i)	$u_{P_i} = \pm 1\%$
Time Uncertainty	$^*u_{\Delta t} = \pm 1$ps
HDR Streak Camera	
Scattered Laser Spectrum	
Timing Accuracy	1ps
Time Resolution	100ps
Time Uncertainty	$u_{\Delta t} = \pm 100$ps
Scattering Calorimeters	
Scattered Laser Power (P_s)	$u_{P_s} = \pm 5\%$
X Ray Framing Camera	
Emitted 1keV x-rays	
Timing Accuracy	5ps
Time Resolution	40ps
Time Uncertainty	$u_{\Delta t} = \pm 30$ps
Ablation Front Position (R)	$u_R = \pm 1.8\%$
Ablation Front Velocity (v)	$u_v = \pm 5\%$

Table 2: Nominal values and uncertainty (1σ) for the experiment and simulation inputs for the direct-drive, single-shell implosion experiments [30]. Uncertainties marked with a * denote best estimates of the uncertainty determined by the validation team.

Quantity	Nominal Value	Uncertainty
Laser		
Number of beams (n_{beams})	60	
Laser Wavelength (λ)	351nm	$^*u_\lambda = \pm 1\%\lambda$
Profile size (r_{beam})	650μm FWHM	$^*u_{r_{beam}} = \pm 1\% r_{beam}$
Gaussian Profile	4th order	NA
Triple-picket timing T		u_T
(low energy)	3x100ps +1x1.6ns square pulse	$^* \pm 1$ps
(high energy)	3x100ps +1x1.2ns square pulse	$^* \pm 1$ps
Energy (E)		
(low energy)	18.5kJ	±0.2kJ
(high energy)	22.9kJ	±0.2kJ
Capsule		
Ablator Materials	CH, Be, C	NA
Density (ρ)	1.03 (CH), 1.83 (Be), 3.35 (C) mg/cm^3	$^*u_\rho = \pm 1\%\rho$
Mass of Shell (m)		u_m
(low energy)	62μg	$\pm 1\mu$g
(high energy)	64μg	$\pm 2\mu$g
Outer Radius of Shell (r)		u_r
(low energy)	440μm	$\pm 10\mu$m
(high energy)	447μm	$\pm 10\mu$m
Internal Gas Temperature (T_1)		$^*u_{T_1} = \pm 1\% T_1$
Internal Gas Density (ρ_1)		$^*u_{\rho_1} = \pm 1\%\rho_1$
Ambient Gas Temperature (T_3)		$^*u_{T_3} = \pm 1\% T_1$
Ambient Gas Density (ρ_3)		$^*u_{\rho_3} = \pm 1\%\rho_3$